

From dwarf spheroidals to cDs: Simulating the galaxy population in a Λ CDM cosmology

Qi Guo^{1,2}*, Simon White¹, Michael Boylan-Kolchin¹, Gabriella De Lucia³, Guinevere Kauffmann¹, Gerard Lemson¹, Cheng Li¹, Volker Springel^{1,4}, Simone Weinmann¹

¹ *Max Planck Institut für Astrophysik, Karl-Schwarzschild-Str. 1, 85741 Garching, Germany*

² *Institute for Computational Cosmology, Department of Physics, University of Durham, South Road, Durham, DH1 3LE, UK*

³ *INAF - Astronomical Observatory of Trieste, via G.B. Tiepolo 11, I-34143 Trieste, Italy*

⁴ *Heidelberg Institute for Theoretical Studies, Schloss-Wolfsbrunnengasse 35, 69118 Heidelberg, Germany*

Accepted ???? ?. 2010 ???? ??

ABSTRACT

We have updated and extended our semi-analytic galaxy formation modelling capabilities and applied them simultaneously to the stored halo/subhalo merger trees of the Millennium and Millennium-II simulations. These differ by a factor of 125 in mass resolution, allowing explicit testing of resolution effects on predicted galaxy properties. We have revised the treatments of the transition between the rapid infall and cooling flow regimes of gas accretion, of the sizes of bulges and of gaseous and stellar disks, of supernova feedback, of the transition between central and satellite status as galaxies fall into larger systems, and of gas and star stripping once they become satellites. Plausible values of efficiency and scaling parameters yield an excellent fit not only to the observed abundance of low-redshift galaxies over 5 orders of magnitude in stellar mass and 9 magnitudes in luminosity, but also to the observed abundance of Milky Way satellites. This suggests that reionisation effects may not be needed to solve the “missing satellite” problem except, perhaps, for the faintest objects. The same model matches the observed large-scale clustering of galaxies as a function of stellar mass and colour. The fit remains excellent down to ~ 30 kpc for massive galaxies. For $M_* < 6 \times 10^{10} M_\odot$, however, the model overpredicts clustering at scales below ~ 1 Mpc, suggesting that the assumed fluctuation amplitude, $\sigma_8 = 0.9$, is too high. The observed difference in clustering between active and passive galaxies is matched quite well for all masses. Galaxy distributions within rich clusters agree between the simulations and match those observed, but only if galaxies without dark matter subhalos (so-called orphans) are included. Even at MS-II resolution, schemes which assign galaxies only to resolved dark matter subhalos cannot match observed clusters. Our model predicts a larger passive fraction among low-mass galaxies than is observed, as well as an overabundance of $\sim 10^{10} M_\odot$ galaxies beyond $z \sim 0.6$. (The abundance of $\sim 10^{11} M_\odot$ galaxies is matched out to $z \sim 3$.) These discrepancies appear to reflect deficiencies in the way star-formation rates are modelled.

Key words: cosmology: theory – cosmology: dark matter mass function – galaxies: luminosity function, stellar mass function – galaxies: haloes – cosmology: large-scale structure of Universe

1 INTRODUCTION

The Λ CDM model has been successful in interpreting a wide variety of observations. These include the cosmic microwave background fluctuations at $z \sim 1000$ (e.g. Dunkley et al. 2009), the large-scale clustering of galaxies in the low-

redshift universe (e.g. Percival 2010), the cosmic shear field measured by weak gravitational lensing (e.g. Fu 2008), the high-redshift power spectrum probed by the Lyman α forest (e.g. Viel et al. 2009; Paschos et al. 2009), and the abundance (e.g. Vikhlinin et al. 2009) and baryon fractions (e.g. Allen et al. 2008) of galaxy clusters. Current N-body simulations can follow the growth of representative samples of dark matter halos at high resolution and in their full cosmologi-

* Email: guoqi@durham.ac.uk

cal context on scales ranging from those of rich clusters to those of dwarf galaxies. The formation of galaxies does not, however, trace that of their dark matter halos in a simple manner, and the exponentially growing body of high-quality galaxy data coming from large surveys cannot be properly compared to the Λ CDM model without a careful treatment of baryonic processes. Such detailed comparison is the most promising route to clarifying the complex astrophysics underlying galaxy formation, and it may also uncover problems with the Λ CDM model which are not evident on larger scales.

In the standard scenario of galaxy formation, originally proposed by White & Rees (1978), gas cools and condenses at the centres of a population of hierarchically merging dark matter haloes. These and earlier ideas (e.g. Rees & Ostriker 1977) were adapted by Blumenthal et al. (1984) to the specific initial conditions predicted in a CDM dominated universe, showing that the dichotomy between rapid and slow cooling regimes provides a natural explanation for the dichotomy between individual galaxies and larger systems like groups and clusters. Within such models, and in particular within the current standard Λ CDM model, dark matter halos grow through accretion and merging to produce a present-day halo mass function which has a very different shape from the observed luminosity function of galaxies (e.g. Benson et al. 2003). If one nevertheless matches the two, assuming bigger galaxies to live in bigger halos, the ratio of halo mass to central galaxy light is found to minimize for galaxies similar to the Milky Way and to increase rapidly for both more massive and less massive systems. The maximal efficiency for converting available baryons into stars is about 20%, and much lower efficiencies are found for the halos of rich clusters or dwarf galaxies (Moster et al. 2010; Guo et al. 2010).

A popular explanation for the low efficiency of galaxy formation in massive halos is that a supermassive black hole releases vast amounts of energy when it accretes gas from its surroundings, and that this suppresses cooling onto (and hence star formation in) the host galaxy (Silk & Rees 1998; Bîrzan et al. 2004; Croton et al. 2006; Bower et al. 2006). For low-mass halos, White & Rees (1978) argued that the supernova-driven winds invoked by Larson (1974) to explain the metallicities of dwarf galaxies might sufficiently reduce the efficiency of galaxy formation. Although this has been the preferred theoretical explanation ever since, there is still no convincing observational evidence that dwarf galaxy winds have the properties needed to reproduce the faint end of the galaxy luminosity function in a Λ CDM universe. Current simulations of dwarf galaxy formation, while predicting substantial winds, nevertheless suppress star formation much less effectively than is required (Sawala et al. 2010). The UV and X-ray backgrounds heat the intergalactic medium and are also thought to affect galaxy formation in small halos (Doroshkevich et al. 1967; Couchman & Rees 1986; Efstathiou 1992; Gnedin 2000; Benson et al. 2002; Hoesft et al. 2006; Okamoto et al. 2008; Hambrick et al. 2009).

A related issue is the *missing satellite* problem. According to the Λ CDM model, the halo of the Milky Way accreted many lower mass halos as it grew, many of which should have contained small galaxies. Just as low-mass isolated halos produce too many dwarf field galaxies unless their galaxy formation efficiency is extremely low, so these

accreted halos overpredict the number of dwarf satellites around the Milky Way unless their star formation is similarly suppressed (Kauffmann et al. 1993). Simulations of the growth of such halos revealed correspondingly large numbers of surviving dark matter subhalos as soon as their resolution was high enough (Klypin et al. 1999; Moore et al. 1999), and increasing resolution has predicted ever larger numbers of ever smaller objects (Diemand et al. 2007; Springel et al. 2008; Boylan-Kolchin et al. 2009). The number of known satellites of the Milky Way has also increased in recent years, through effective use of the Sloan Digital Sky Survey (SDSS) to detect extremely low luminosity systems (Willman et al. 2005; Zucker & et al. 2006; Belokurov & et al. 2007; Koposov et al. 2008), but the apparent discrepancy between the predicted and observed numbers has steadily grown. Environmental effects undoubtedly play a role in determining satellite properties: after a galaxy falls into a larger system, its gas may be stripped, leading to a rapid decline in star formation, dimming its light and reddening its colour. Tidal stripping may remove stars or even destroy the satellite altogether, contributing gas to the disk of the central galaxy and stars to its stellar halo. Nevertheless, since the subhalos survive in the simulations, such disruption cannot explain the apparent discrepancy. Many low-mass subhalos must be dark if the Λ CDM model is correct.

An entirely different resolution of these problems could lie in a modification of the Λ CDM model itself. A number of authors have suggested that the suppression of small-scale structure expected in a warm dark matter model might reduce the abundance of low-mass halos enough to alleviate the tension (e.g. Bode et al. 2001; Zavala et al. 2009; Macciò et al. 2010). The strongest constraint on this low-mass cut-off currently comes from observations of small-scale structure in the high-redshift intergalactic medium, as observed through the Ly α forest in quasar spectra. These place an upper limit on the cut-off wavelength and the corresponding halo mass, which implies a lower limit on the mass of the dark matter particle (Viel et al. 2008; Boyarsky et al. 2009a,b). Taken at face value, this recent work appears to exclude significant warm dark matter effects on any but the very faintest galaxies.

In recent years, the completion of SDSS has allowed a determination of the galaxy stellar mass function down to a stellar mass of $10^7 M_{\odot}$. Above about $10^8 M_{\odot}$ these mass functions are robust against incompleteness and cosmic variance and have very small uncertainties, other than an overall systematic coming from the poorly known stellar initial mass function (Baldry et al. 2008; Li & White 2009). The large sample size makes it possible to retain small mass function errors for subsamples split according to additional galaxy properties such as colour and environment (Peng & et al. 2010). This results in a considerable sharpening of the constraints on galaxy formation within the Λ CDM model (Guo et al. 2010; Sawala et al. 2010), making it timely to reassess the viability of current models, in particular their ability to reproduce the faint end of the galaxy luminosity (or stellar mass) function and the faint satellite abundance around the Milky Way.

In this paper we use the combination of the Millennium Simulation (MS, Springel et al. 2005) and the Millennium-II Simulation (MS-II, Boylan-Kolchin et al. 2009) to address this issue. The latter has 125 times better mass res-

olution and 5 times better force resolution than the MS, but follows evolution within a box of 5 times smaller side. We update our earlier MS-based galaxy formation models (Springel et al. 2005; Croton et al. 2006; De Lucia & Blaizot 2007, hereafter collectively referred to as DLB07) to include a better treatment of a number of physical processes, and we apply the improved model to both simulations simultaneously. This allows us to test explicitly how limited resolution affects our results. We demonstrate that together, the two simulations enable study of the formation, evolution and clustering of galaxies ranging from the faint dwarf satellites of the Milky Way to the most massive cD galaxies. Uncertain astrophysical processes are strongly constrained by the precise, low-redshift abundance and clustering data provided by the SDSS. Models consistent with these data can be tested against other observational data, notably the satellite abundance around the Milky Way, but also, for example, the Tully-Fisher relations of giant and dwarf galaxies or the properties of high-redshift galaxy populations.

Previous generations of semi-analytic galaxy formation models have been able to reproduce the properties of observed galaxy populations in ever increasing detail (White & Frenk 1991; Kauffmann et al. 1993; Cole et al. 1994; Kauffmann et al. 1999; Somerville & Primack 1999; Cole et al. 2000; Springel et al. 2001; Hatton et al. 2003; Kang et al. 2005; Baugh et al. 2005; Croton et al. 2006; Bower et al. 2006; De Lucia & Blaizot 2007; Somerville et al. 2008; Font et al. 2008; Guo & White 2009; Weinmann et al. 2009). The DLB07 model was built for the MS simulation and has been extensively compared to the abundance, intrinsic properties and clustering of galaxies, both in the local universe and at high redshift. These comparisons have generally been limited to galaxies with stellar masses of at least $10^9 M_\odot$, corresponding approximately to the resolution limit of the MS. When the same model is applied to the MS-II, it significantly overpredicts the observed abundance of galaxies near this limit and it substantially overpredicts the abundance at lower masses (see Fig. 1). The high-mass cut-off is also at slightly larger mass than in the new SDSS data, although it was consistent with earlier datasets (Croton et al. 2006). Clearly, galaxy formation efficiencies are substantially too high at low halo mass in the DLB07 model, and slightly too high at high halo mass (see also, for example, Fontanot et al. 2009)

In the following section, we revisit the DLB07 model, improving the treatment of a number of physical processes and retuning the uncertain efficiency parameters to obtain a better fit to the new SDSS data on abundance and clustering. In particular, we change the treatments of supernova feedback, of the reincorporation of ejected gas, of the sizes of galaxies, of the distinction between satellite and central galaxies, and of environmental effects on galaxies. Our paper is organised as follows. In Sec. 2 we briefly describe the two N-body simulations on which we implement our galaxy formation model. A detailed description of the semi-analytic model itself is presented in Sec. 3. In Sec. 4 we compare both the abundance and the clustering of galaxies as a function of stellar mass, luminosity and colour to low-redshift data from the SDSS. We also compare model predictions to the observed abundance of satellite galaxies around the Milky Way, to the Tully-Fisher relation of isolated galaxies, and to the galaxy number density profiles, stellar mass functions,

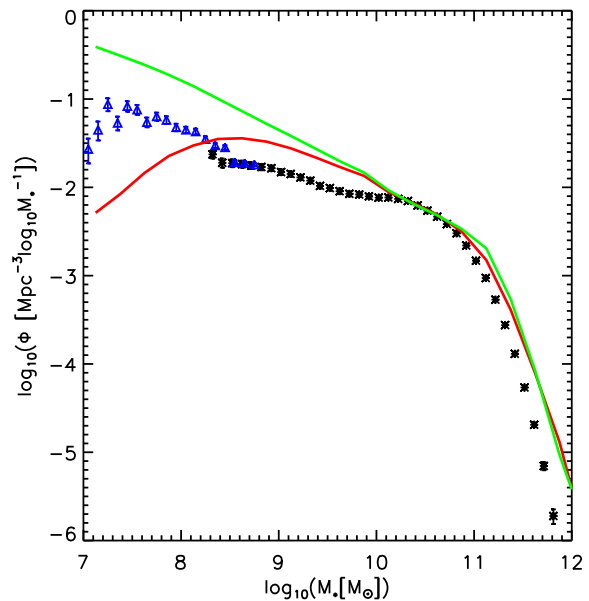


Figure 1. Stellar mass functions predicted by the galaxy formation model of DLB07. The green curve is the prediction for the MS-II and the red curve is that for the MS. Results for the two simulations agree well above $10^{9.5} M_\odot$, but resolution effects cause an underprediction at lower masses in the MS. Black stars show the observed function for SDSS/DR7 with error bars including both counting and cosmic variance uncertainties (Li & White 2009; Guo et al. 2010). Blue triangles are results for a low-redshift sample ($0.0033 < z < 0.05$) from SDSS/DR4 taken from Baldry et al. (2008); these are corrected for surface-brightness incompleteness, but the error bars do not include cosmic variance uncertainties. Clearly the model substantially overpredicts the abundance of low-mass galaxies and slightly overpredicts the masses of high-mass galaxies.

and intergalactic light fractions of clusters. A final subsection focusses on a few model predictions at high redshift. Sec. 5 presents a concluding discussion of our results.

2 N-BODY SIMULATIONS

We build virtual catalogues of the galaxy population by implementing galaxy formation models on the stored output of two very large cosmological N-body simulations, the Millennium Simulation (MS, Springel et al. 2005) and the Millennium-II Simulation (MS-II Boylan-Kolchin et al. 2009). Both simulations assume a Λ CDM cosmology with parameters based on a combined analysis of the 2dFGRS (Colless & et al. 2001) and the first-year WMAP data (Spergel et al. 2003). The parameters are $\Omega_m = 0.25$, $\Omega_b = 0.045$, $\Omega_\Lambda = 0.75$, $n = 1$, $\sigma_8 = 0.9$ and $H_0 = 73 \text{ km s}^{-1} \text{ Mpc}^{-1}$. These cosmological parameters are not consistent with more recent analyses of the CMB data (e.g. Komatsu et al. 2010) but the relatively small off-sets are not significant for most of the issues addressed in this paper, with the important exception of the small-scale clustering analysis of section 4.9.) The parameter which deviates most from recent estimates is σ_8 which is quoted as

0.809±0.024 for WMAP7 by Komatsu et al. (2010), disagreeing with the simulation value by almost 4σ . As shown by Angulo & White (2010) simulations based on the MS cosmology can be scaled to represent neighboring cosmologies such as WMAP7 to the precision needed for making galaxy catalogues. In future work we will use this to show how predictions for galaxy properties are affected by the small parameter shifts to WMAP7 and other currently allowed cosmologies.

Both MS and the MS-II trace 2160^3 particles from redshift 127 to the present day. The MS was carried out in a periodic box of side 685 Mpc and the MS-II in a box of side 137 Mpc. The corresponding particle masses are $1.18 \times 10^9 M_\odot$ and $9.45 \times 10^6 M_\odot$, respectively. The smallest halos/subhalos we consider contain 20 bound particles, and it will turn out that the MS-II has just sufficient resolution to study dwarf galaxies as faint as those seen around the Milky Way. On the other hand, the large volume of the MS makes it possible to study rare objects like rich clusters and bright quasar hosts. In addition, a comparison of the two simulations where both have good statistics allows us to study how the limited resolution of the MS affects its model galaxy populations.

The particle data were stored at 64 and 68 times for the MS and the MS-II, respectively, with the last 60 being identical in the two simulations. At each output time, the post-processing pipeline produced a friends-of-friends (FOF) catalogue by linking particles with separation less than 0.2 of the mean value (Davis et al. 1985). The SUBFIND algorithm (Springel et al. 2001) was then applied to each FOF group to identify all its bound substructures (subhalos). The merger trees which are the basis for our galaxy formation modelling are then constructed by linking each subhalo found in a given output to one and only one descendent at the following output (Springel et al. 2005; De Lucia & Blaizot 2007; Boylan-Kolchin et al. 2009). Note that all our galaxy formation models are thus based on the growth and merging of the population of *subhalos*, not on the growth and merging of the population of *halos*. This is an important distinction which allows us to build much more realistic models for the galaxy population, in particular for its merging rates and its clustering, than would otherwise be the case. We refer readers to Springel et al. (2005) and Boylan-Kolchin et al. (2009) for full descriptions of the two simulations.

The most massive self-bound subhalo in a FOF group is referred to as its main subhalo (sometimes the main halo) and usually contains most of its mass. Other subhalos of the FOF group are referred to as satellite subhalos. After implementation of the galaxy formation model, each FOF group hosts a “central galaxy”, which sits at the potential minimum of the main subhalo. Other associated galaxies may sit at the potential minima of smaller subhalos, or may no longer correspond to a resolved dark matter substructure (“orphans”). These galaxies are collectively referred to as satellites, although we note that in this paper we break with our previous practice by assuming that the physical processes affecting satellite galaxies only begin to differ from those affecting central galaxies when a satellite first enters the virial radius of the larger system. This is to account for the fact that FOF groups quite often link two essentially independent dark matter clumps, and the two central galaxies

are expected to keep evolving quasi-independently while this is the case.

We define the centre of a FOF group to be its potential minimum and its virial radius to be the radius of the largest sphere with this centre and a mean overdensity exceeding 200 times the critical value. The total mass within the virial radius is defined as the virial mass of the group. Virial radius and virial mass are then related by

$$R_{\text{vir}} = \left(\frac{G}{100} \frac{M_{\text{vir}}}{H^2(z)} \right)^{1/3}. \quad (1)$$

The virial radius usually lies almost entirely within the boundary of the FOF group and, as a result, the virial mass is typically somewhat smaller than the FOF mass (and also typically somewhat larger than the mass of the main subhalo).

3 GALAXY FORMATION MODELS

Galaxies form at the centres of dark matter halos and gain stars by formation from their interstellar medium (ISM) and by accretion of satellite galaxies. We assume the ISM to form a disk and to be replenished both by diffuse infall from the surroundings and by gas from accreted satellite galaxies. Diffuse infall can occur directly from the intergalactic medium (in a so-called “cold flow”) or through cooling of a hot halo surrounding the galaxy. The interaction of these processes with each other and with flows driven by supernovae and by active galactic nuclei is responsible for the overall evolution of each galaxy, which thus cannot be followed realistically without superposing a complex network of baryonic astrophysics on the assembly history of its dark matter component. Physical understanding of most of these baryonic processes is quite incomplete and is based largely on simplified numerical simulations and on the phenomenology of observed systems. Descriptions of the processes are thus necessarily both approximate and uncertain, and models of the kind we build here may offer the best means to constrain them empirically using observational data.

Here we implement simplified galaxy formation recipes onto the subhalo merger trees built from the MS and the MS-II. Treating baryonic evolution by post-processing cosmological N-body simulations in this way makes it possible to explore a wide model and parameter space in a relatively short amount of time. In general, our models build on those developed in Springel et al. (2005), Croton et al. (2006), and De Lucia & Blaizot (2007) hereafter collectively referred to as DLB07. The baryonic content of galaxies is split into five components, a stellar bulge, a stellar disk, a gas disk, a hot gas halo, and an ejecta reservoir. These components exchange material through a variety of processes and their total mass grows through accretion from the intergalactic medium. As noted above the main modifications here concern the definition of satellite galaxies, a mass-dependent model for supernova feedback, the gradual stripping and disruption of satellite galaxies, more realistic treatments of the growth of gaseous and stellar disks, a model to calculate bulge and elliptical galaxy sizes, and an updated reionization model. We determine the free parameters of these models using the observed abundance, structure and clustering of low redshift galaxies as a function of stellar mass,

luminosity and colour. In the following we describe our new galaxy formation model in detail. For a more general review of semi-analytic models, we refer the reader to Baugh (2006); Benson & Bower (2010b); Benson (2010)

3.1 Reionization

It is now well established that the global baryon to dark matter mass ratio is 15-20%. In galaxy clusters, the observed baryon fraction is close to but somewhat below this value, and is mostly in the form of hot gas. In halos like that of the Milky Way, on the other hand, at most about 20% of the expected baryons are detected and these are primarily in the form of stars; the detected baryon fraction is apparently even lower in the halos of dwarf galaxies (e.g. Guo et al. 2010). One mechanism which may contribute to the low efficiency of dwarf galaxy formation is photo-heating of pregalactic gas by the UV background. This inhibits gas condensation within dark matter halos if the thermal energy exceeds the halo potential well depth. This effect was first pointed out by Doroshkevich et al. (1967) and was later investigated in the context of CDM models by Couchman & Rees (1986) and Efstathiou (1992).

In recent years a number of simulations of this process have been carried out. Here we use a fitting function of the form originally proposed by Gnedin (2000) to describe how the baryon fraction in a halo depends on mass and redshift:

$$f_b(z, M_{\text{vir}}) = f_b^{\text{cos}} \left(1 + (2^{\alpha/3} - 1) \left[\frac{M_{\text{vir}}}{M_F(z)} \right]^{-\alpha} \right)^{-3/\alpha}. \quad (2)$$

In this formula, $f_b^{\text{cos}}=17\%$ is the universal baryon fraction as given by first-year WMAP estimates (Spergel et al. 2003), and $\alpha = 2$ is a fit to the simulations in Okamoto et al. (2008). M_F is the characteristic halo mass of this ‘‘filter’’. In halos with $M_{\text{vir}} \gg M_F(z)$ the baryon fraction is set to the universal value, while in halos with $M_{\text{vir}} \ll M_F(z)$ it drops as $(M_{\text{vir}}/M_F)^3$. The redshift dependence of M_F is determined by the details of how the reionization process occurred. Here we use a table of $M_F(z)$ kindly provided by Okamoto et al. (2008) from their simulations; M_F varies from $\sim 6.5 \times 10^9 M_\odot$ at $z = 0$ to $\sim 10^7 M_\odot$ just after reionization at $z \sim 8$. These results are consistent with those found earlier by Hoefl et al. (2006). In DLB07, a lower value of α and a different $M_F(z)$ were adopted (following Kravtsov et al. 2004) leading to the substantially higher value $M_F \sim 3 \times 10^{10} M_\odot$ at $z = 0$. These differences in simulation results appear to reflect differences in resolution and in the treatment of radiative transfer. Although we adopt the more recent results as ‘‘standard’’, we will rediscuss how these issues affect dwarf galaxy formation in Sec. 4.8, showing that reionization does not appear to be a major factor except, possibly, for the faintest Milky Way satellite systems.

3.2 Cooling

The pressure of the intergalactic medium has little effect on the growth of more massive halos. A fraction $\sim f_b^{\text{cos}}$ of the infalling material is expected to be diffuse gas, and thus must shock as it joins the halo. At early times and in low-mass halos, post-shock cooling is rapid and the accretion shock is very close to the central object, which thus

gains new material at essentially the free-fall rate; at late times and in massive halos, post-shock cooling times exceed halo sound crossing times, the accretion shock moves away from the galaxy, and infalling gas forms a quasi-static hot atmosphere from which it condenses onto the central galaxy through a cooling flow (Forcada-Miro & White 1997; Birnboim & Dekel 2003). The critical mass separating these two regimes is around $10^{12} M_\odot$ and is weakly dependent on redshift but strongly dependent on f_b^{cos} and on the metallicity of the infalling gas (Rees & Ostriker 1977; White & Frenk 1991). These rapid infall and quasi-static cooling flow regimes have featured in almost all galaxy formation models of the last two decades (e.g. Kauffmann et al. 1993; Cole et al. 1994; Kauffmann et al. 1999; Somerville & Primack 1999; Cole et al. 2000; Springel et al. 2001; Hatton et al. 2003; Kang et al. 2005; Somerville et al. 2008, and also, of course DLB07) as well as (by construction) in all direct simulations of the galaxy formation process (e.g. Navarro & Steinmetz 1997; Steinmetz 1999; Springel & Hernquist 2003). The simple criterion of White & Frenk (1991) is used to separate the two regimes in most semi-analytic models, and tests with both one-dimensional (Forcada-Miro & White 1997) and three-dimensional (Benson et al. 2001; Yoshida et al. 2002; Cattaneo et al. 2007) simulations have shown it to provide an adequate description. More recent numerical work has focussed on the fact that the two regimes can effectively coexist near the transition, with cold gas falling in narrow streams through a hot gas atmosphere or even a galactic wind (see, for example, Fig.2 of Springel & Hernquist (2003) or Dekel et al. (2009)). A recent reanalysis by Benson & Bower (2010a) emphasised that the details of how such ‘‘cold flows’’ are treated has little effect on predicted galaxy properties once the necessary strong feedback is included.

Here we use the simple model of Springel et al. (2001) to estimate the gas cooling rate in the hot halo regime. We assume that infalling gas is shock-heated to the virial temperature of the host halo at an accretion shock, and that its distribution interior to this shock is a quasistatic isothermal sphere with density falling as the inverse square of radius. The cooling time at each radius can then be calculated as

$$t_{\text{cool}}(r) = \frac{3\mu m_{\text{H}} k T_{\text{vir}}}{2\rho_{\text{hot}}(r)\Lambda(T_{\text{hot}}, Z_{\text{hot}})}, \quad (3)$$

where μm_{H} is the mean particle mass, k is the Boltzmann constant, $\rho_{\text{hot}}(r)$ is the hot gas density at radius r , $\Lambda(T_{\text{hot}}, Z_{\text{hot}})$ is the temperature- and metallicity-dependent cooling function (Sutherland & Dopita 1993), and Z_{hot} is the metallicity of the hot halo gas. $T_{\text{hot}} = 35.9(V_{\text{vir}}/\text{km s}^{-1})^2 \text{K}$ is the assumed virial temperature of the host halo. For main subhalos, the gas temperature is updated according to the current circular velocity at the virial radius at each snapshot, while for satellite subhalos, we assume the gas temperature to be constant at the value it had when the subhalo was accreted onto its main halo.

The cooling radius is then estimated through

$$r_{\text{cool}} = \left[\frac{t_{\text{dyn,h}} m_{\text{hot}} \Lambda(T_{\text{hot}}, Z_{\text{hot}})}{6\pi \mu m_{\text{H}} k T_{\text{vir}} R_{\text{vir}}} \right]^{\frac{1}{2}}. \quad (4)$$

The definition of the halo dynamical time $t_{\text{dyn,h}}$ involves an arbitrary constant. Here we adopt the convention $t_{\text{dyn,h}} \equiv R_{\text{vir}}/V_{\text{vir}} = 0.1H(z)^{-1}$ as in De Lucia et al. (2004). Readers

are referred to Croton et al. (2006) and Somerville et al. (2008) for the discussion of other possible choices of $t_{\text{dyn,h}}$ when defining r_{cool} . When $r_{\text{cool}} < R_{\text{vir}}$, we assume that we are indeed in the cooling flow regime, and that the cooling rate onto the central galaxy is¹

$$\dot{M}_{\text{cool}} = m_{\text{hot}} \frac{r_{\text{cool}}}{R_{\text{vir}}} \frac{1}{t_{\text{dyn,h}}}. \quad (5)$$

When $r_{\text{cool}} > R_{\text{vir}}$, on the other hand, we assume that we are in the rapid infall regime and gas accretes onto the central object in free-fall, thus on the halo dynamical time:

$$\dot{M}_{\text{cool}} = \frac{m_{\text{hot}}}{t_{\text{dyn,h}}}. \quad (6)$$

Note that condensation is smoother in time in this model (which is essentially identical to that of De Lucia et al. (2004)) than in the model of DLB07, who assumed the hot gas to fall onto the central object instantaneously as soon as it satisfies $r_{\text{cool}} > R_{\text{vir}}$. In a situation of steady accretion onto a low-mass halo, the DLB07 model results in non-steady behaviour; after a cooling “event” empties the halo, its hot gas atmosphere is replenished by infall until it again reaches the rapid cooling threshold, triggering another cooling event. Although the time-average condensation rate is equal to the infall rate onto the halo, condensation occurs in bursts which induce (possibly) unrealistic star formation bursts in the central object. The model of Equ. (6) eliminates this behaviour. For a low-mass halo experiencing steady infall, condensation onto the central object is now also steady, and the hot gas atmosphere has constant mass equal to the gas infall rate times the halo dynamical time. The coefficient of unity in Equ. (6) ensures continuity of the condensation rate as a halo transitions between the rapid infall and hot halo regimes. With these changes, condensation rates onto galaxies fluctuate strongly only in response to variations in the accretion onto their halos, not as a consequence of discontinuities in the way we treat the various regimes.

Another substantive difference in the way we treat cooling with respect to the model of DLB07 is that we now allow satellite galaxies to have their own hot gas halos which can be removed dynamically by tidal and ram-pressure effects. This hot gas can continue to cool onto the (satellite) galaxy, adding to its interstellar medium and providing additional fuel for star formation. We discuss this in more detail in sect. 3.6 below.

3.3 Disk Sizes

Disk sizes are not only interesting in their own right, but are also important because they determine the surface density

¹ Note that the coefficient on the *rhs* of this equation differs from that in the corresponding equation (equ. 6) of Croton et al. (2006). By checking the original code, we have verified that a factor of 0.5 was erroneously omitted when programming equ. 6 in this paper, and that this error then propagated through all the later DLB07 papers, with the result that the equations which actually correspond to the models of Croton et al. (2006) and DLB07 are those given here. For consistency in comparing to the earlier work, we have kept these assumptions in our new model.

of gas in disks, which in turn determines the star formation rate. DLB07 followed the simple model of Mo et al. (1998) which assumes that the specific angular momentum of a galaxy disk is the same as that of the dark halo in which it is embedded. This results in the characteristic size of a disk scaling as the product of the virial radius and the spin parameter of its host halo. Mo et al. (1998) intended this as a simple model for a population of isolated disk galaxies at a single time, and several difficulties arise when it is applied to individual objects as they grow in time. For example, halo spin parameters often change discontinuously by quite large amounts as new material is accreted, but it is not plausible that this should result in instantaneous changes in size of the central disk. Here we introduce a new and more realistic disk model which distinguishes between gas and stellar disks and allows each of them to grow continuously in mass and angular momentum in a physically plausible way.

We assume that the change in the total vector angular momentum of the gas disk during a timestep can be expressed as

$$\Delta \vec{J}_{\text{gas}} = \delta \vec{J}_{\text{gas,cooling}} + \delta \vec{J}_{\text{gas,acc}} + \delta \vec{J}_{\text{gas,SF}}, \quad (7)$$

where $\delta \vec{J}_{\text{gas,cooling}}$, $\delta \vec{J}_{\text{gas,acc}}$ and $\delta \vec{J}_{\text{SF}}$ are respectively the angular momentum changes due to addition of gas by cooling, to accretion from minor mergers, and to gas removal through star formation.

When new gas condenses onto the central galaxy, we assume it to carry specific angular momentum which matches the current value for the dark matter halo $\vec{J}_{\text{DM}}/M_{\text{DM}}$. The angular momentum change due to this gas can thus be expressed as

$$\delta \vec{J}_{\text{gas,cooling}} = \dot{M}_{\text{cool}} \frac{\vec{J}_{\text{DM}}}{M_{\text{DM}}} \delta t, \quad (8)$$

where \dot{M}_{cool} is the condensation rate from Equ. (5) or Equ. (6), and δt is the timestep. When a minor merger happens (which we define as the smaller galaxy having a baryonic mass less than a third that of the larger) we assume the cold gas from the smaller object to be added to the disk of the larger (see Sec. 3.7), carrying specific angular momentum equal to the current value for the dark matter halo of the larger object. The corresponding angular momentum change in the gas disk is thus

$$\delta \vec{J}_{\text{gas,acc}} = M_{\text{sat,gas}} \frac{\vec{J}_{\text{DM}}}{M_{\text{DM}}}, \quad (9)$$

where $M_{\text{sat,gas}}$ is the cold gas mass in the satellite disk.

When some gas from the cold disk is converted into stars, we assume it to have the average specific angular momentum of the gas disk, $\vec{J}_{\text{gas}}/M_{\text{gas}}$, so the change in angular momentum of the gas and stellar disks is

$$\delta \vec{J}_{\text{gas,SF}} = -\dot{M}_{*} \frac{\vec{J}_{\text{gas}}}{M_{\text{gas}}} \delta t = -\delta \vec{J}_{*,\text{SF}}, \quad (10)$$

where \dot{M}_{*} is the star formation rate.

When the cold gas in disks is reheated by SN feedback, we assume that the outflowing material also carries away its “fair share” of the angular momentum. As a result, the specific angular momentum of the gas disk is not changed by the SN feedback process.

For the stellar disk, we assume the *total* change in (vector) angular momentum over the timestep to be $\delta \vec{J}_{*,\text{SF}}$. Thus

we are assuming that the angular momentum of the disk is changed *only* by star formation. In particular, bulge formation through disk instability (see Sect. 3.8) is assumed to remove negligible angular momentum from the disk.

We assume both the gas disk and the stellar disk to be thin, to be in centrifugal equilibrium and to have exponential density profiles

$$\Sigma(R_{\text{gas}}) = \Sigma_{\text{gas}0} \exp(-R_{\text{gas}}/R_{\text{gas,d}}), \quad (11)$$

and

$$\Sigma(R_*) = \Sigma_{*0} \exp(-R_*/R_{*,d}), \quad (12)$$

where $R_{\text{gas,d}}$ and $R_{*,d}$ are the scale-lengths of the gas and stellar disks, and $\Sigma_{\text{gas}0}$ and Σ_{*0} are the corresponding central surface densities. Assuming a flat circular velocity curve, as would hold for a galaxy with negligible self-gravity in an isothermal dark matter halo, the scale-lengths can be calculated as

$$R_{\text{gas,d}} = \frac{J_{\text{gas}}/M_{\text{gas}}}{2V_{\text{max}}}, \quad (13)$$

and

$$R_{*,d} = \frac{J_*/M_{*,d}}{2V_{\text{max}}}, \quad (14)$$

where M_{gas} and $M_{*,d}$ are the total masses of the two disks. A significant issue here is the dark matter response to the gravity of the baryons as they condense within the halo. The simplest model for this effect assumes adiabatic contraction within a spherical halo (e.g. Barnes 1984; Blumenthal et al. 1986) and has often been adopted in galaxy formation models (e.g. Mo et al. 1998; Cole et al. 2000). However, recent simulations suggest that this simple scheme overestimates the effect (e.g. Gnedin et al. 2004; Abadi et al. 2010). Most recently, Tissera et al. (2010) found disk maximum rotation velocities very similar to the maximum circular velocities found for dark matter only haloes formed from identical Λ CDM initial conditions. Here, for simplicity, we adopt V_{max} , the maximum circular velocity of the surrounding dark matter halo, as the typical rotation velocity for both stellar and HI disks. Note that we keep the rotation velocities of satellite galaxies fixed after infall. This is because the inner regions of the dark matter subhalo, which determine the rotation velocity of the disks, change rather little until the subhalo is about to be destroyed (e.g. Hayashi et al. 2003; Kazantzidis et al. 2004).

Fig. 2 shows a few results for this simple model implemented on the MS-II to demonstrate that it gives results in fair agreement with observation. The first panel compares model predictions for the distribution of stellar half-mass radius for disk galaxies as a function of their stellar mass to observational results from the Sloan Digital Sky Survey (SDSS, Shen et al. 2003). This SDSS study defined ‘‘late-type’’ galaxies according to the concentration parameter $c = R_{90}/R_{50}$, where R_{50} and R_{90} are the radii which enclose 50% and 90% of the projected stellar light. Galaxies with $c < 2.86$ were taken to be late-type, primarily spiral galaxies. To calculate R_{50} and R_{90} for our model galaxies, we assume the above exponential model for the disk and a Jaffe profile for the bulge (the modelling of bulge size will be described in Sec. 3.8). In practice, $c < 2.86$ corresponds roughly to galaxies with $M_{*,d}/M_{*,\text{tot}} > 0.80$ in our model. The solid curves in the figure show the median and

$\pm 1\sigma$ range of the model distribution as a function of stellar mass, while the symbols show the SDSS data. The amplitude, slope and scatter of the observations are all fairly well reproduced, although the predicted slope is somewhat shallower than observed.

The second panel of Fig. 2 shows the distribution of the ratio of the sizes of the gas and stellar disks. It gives the median, the upper and lower quartiles and the upper and lower 10% points as a function of stellar mass for the same model galaxies plotted in the first panel of the figure. Gas disks are typically larger than stellar disks by about a factor of 1.6 but the scatter in the ratio is large. This agrees quite well with the observational situation. For the WHISP sample of Noordermeer et al. (2005) the average ratio of disk sizes is 1.72 and values within their sample of 49 galaxies range from 0.6 to 4.1.

The third panel of Fig. 2 shows the distribution of the misalignment angle $\theta = \arccos(\vec{J}_{\text{gas}} \cdot \vec{J}_*/|\vec{J}_{\text{gas}}||\vec{J}_*|)$ between the two disks for several ranges of stellar mass, again for the same galaxies. The distribution of misalignment angles is quite broad and seems to depend very little on stellar mass. Warps are quite often seen in the outer parts of spiral galaxies, particularly when the outer HI distribution is compared to the inner stellar disk. The structure and evolution of the two components is quite strongly coupled (e.g. Binney & Tremaine (2008) section 6.6), but our simple model nevertheless gives some indication of the extent to which misalignments might reflect changes with time in the orientation of accreted angular momentum.

3.4 Star Formation

In this paper we assume stars to form from cold gas in the disk according to a simplified version of the empirical relation which Kennicutt (1998) found to give a good description of galaxy-scale star formation in the bulk of low-redshift star-forming galaxies. Stars form efficiently only in regions where the surface mass density exceeds a critical value which is plausibly related to the Toomre (1964) threshold for local instability of a rotationally supported disk. Toomre’s criterion is a function of local velocity dispersion, of the surface densities of stars and gas, and of the local rotation curve. We adopt a simple model which assumes a flat rotation curve and a gas velocity dispersion which is everywhere 6 km/s, leading to the critical surface density suggested in Kauffmann (1996) and Croton et al. (2006),

$$\Sigma_{\text{crit}}(R) = 12 \times \left(\frac{V_{\text{max}}}{200\text{km/s}} \right) \left(\frac{R}{10\text{kpc}} \right)^{-1} M_{\odot}\text{pc}^{-2}. \quad (15)$$

We integrate this out to three exponential scale radii $R_{\text{gas,d}}$ and then divide by a factor of 2 to obtain a critical gas mass which is required for any stars to form

$$M_{\text{crit}} = 11.5 \times 10^9 \left(\frac{V_{\text{max}}}{200\text{km/s}} \right) \left(\frac{R_{\text{gas,d}}}{10\text{kpc}} \right) M_{\odot}. \quad (16)$$

The final reduction by a factor of 2 is introduced to agree with the assumptions of Croton et al. (2006) who took the cold gas surface density to be constant with radius in disks at threshold.

The amount of cold disk gas that is converted into long-lived stars per unit time is assumed to be

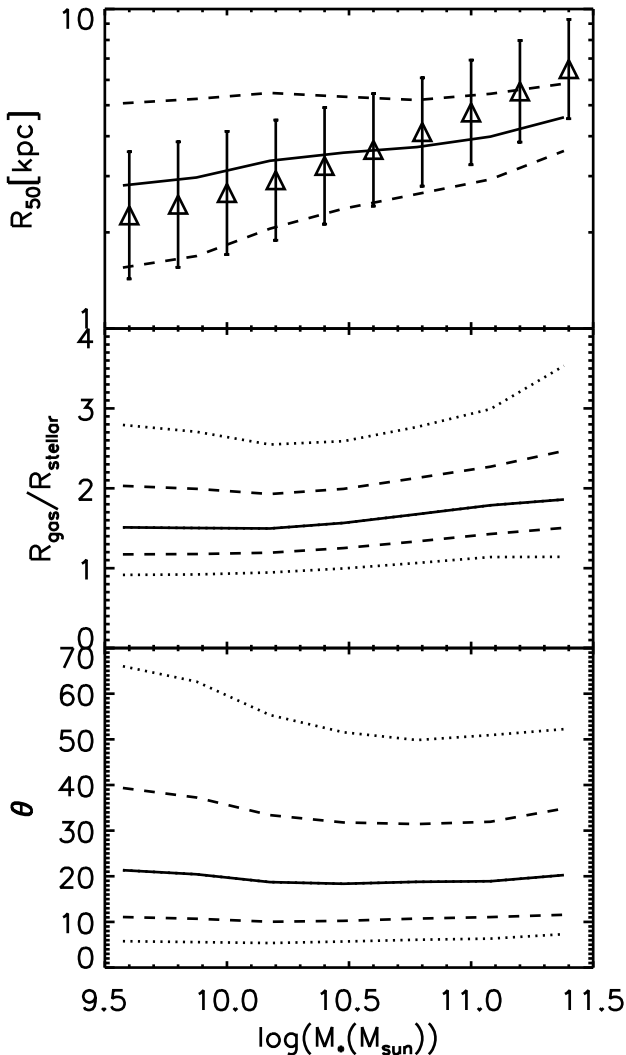


Figure 2. The top panel gives the distribution of the radius containing half the stellar mass as a function of stellar mass for local late-type galaxies. These are defined as having SDSS concentration parameter $c < 2.86$ (see details in the text). The solid curve is the median half-mass radius predicted by our model applied to the MS-II, while dashed curves indicate the *rms* scatter in $\log R$ at each stellar mass. Symbols are the observed median and scatter from the SDSS study by Shen et al. (2003). The central panel gives the 10, 25, 50, 75 and 90% points of the distribution of the ratio of sizes of the gaseous and stellar disks in our model, also as a function of total stellar mass, while the bottom panel shows the same percentile points of the distribution of the relative inclination of the two disks.

$$\dot{M}_* = \alpha(M_{\text{gas}} - M_{\text{crit}})/t_{\text{dyn}} \quad (17)$$

where $t_{\text{dyn}} = 3R_{\text{gas,d}}/V_{\text{max}}$ is the characteristic timescale at the edge of the star-forming disk, and α is an adjustable efficiency parameter. We will adopt $\alpha = 0.02$, which results in a few percent of the gas in a disk being converted into stars each rotation period. The star formation rates implied by this model are, in the mean, quite similar to those in DLB07, but our revised treatments of cooling and of disk size lead to considerably smoother evolution than before,

with less “bursty” star formation histories in the bulk of the galaxy population.

3.5 Supernova Feedback

During their short lives, massive stars emit large amounts of radiation through optical and UV emission, and large amounts of mechanical energy through their winds. As they die, comparable amounts of radiative and mechanical energy are liberated by the final supernova (SN) explosion. This can dramatically reshape the surrounding interstellar medium, ionising and heating it, and in many cases driving galactic-scale winds. Such effects are generically referred to as SN feedback. As Larson (1974) showed, they can have a major impact on the evolution of low-mass galaxies, determining, for example, their metallicities. White & Rees (1978) argued that such SN feedback may induce the strong dependence of galaxy formation efficiency on halo mass required to explain why most stars live in galaxies with stellar mass close to the upper limit imposed by cooling constraints, and why the overall conversion of baryons into stars is relatively inefficient. These ideas have subsequently been explored by many authors, particularly in the context of understanding the shape of the galaxy luminosity function at low luminosities (e.g. Benson et al. 2003). Here we assume that SN feedback injects gas from the cold disk into the hot halo and, in addition, can transfer halo gas to the ejecta reservoir.

We estimate the amount of cold disk gas that is reheated by SN feedback and injected into the hot halo component as

$$\delta M_{\text{reheat}} = \epsilon_{\text{disk}} \times \delta M_*. \quad (18)$$

where δM_* is the mass of newly formed long-lived stars. DLB07 took ϵ_{disk} to be a constant, based on some observational indications that mass outflow rates are typically a few times the star formation rate in actively star-forming galaxies. We find that this scaling does not suppress star formation in low-mass galaxies enough to reproduce the shallow slope of the observed stellar mass function, so we have extended it to allow higher ejection efficiencies in dwarf galaxies, taking

$$\epsilon_{\text{disk}} = \epsilon \times \left[0.5 + \left(\frac{V_{\text{max}}}{70 \text{ km/s}} \right)^{-\beta_1} \right], \quad (19)$$

where ϵ and β_1 are free parameters describing the ratio of reheated mass to new stellar mass in massive galaxies, and the scaling of this ratio with V_{max} in dwarfs. The circular velocity dependence is motivated by the fact that less energy is needed to heat a solar mass of gas to the halo virial temperature and to eject it from the disk in lower mass galaxies. A naive argument leads to the expectation $\beta_1 \sim 2$, but a variety of factors could lead to a different dependence, so we adjust both β_1 and ϵ when fitting to observations, in particular to the observed stellar mass function. Below we will take $\epsilon = 6.5$ and $\beta_1 = 3.5$ in our standard model.

We parametrise the total amount of energy effectively injected by massive stars into disk and halo gas as:

$$\delta E_{\text{SN}} = \epsilon_{\text{halo}} \times \frac{1}{2} \delta M_* V_{\text{SN}}^2. \quad (20)$$

where $0.5V_{\text{SN}}^2$ is the mean kinetic energy of supernova ejecta

per unit mass of stars formed, and, following Croton et al. (2006), we take $V_{\text{SN}} = 630\text{km/s}$, based on standard assumptions for the stellar initial mass function and the energetics of SN explosions. In this case also, DLB07 assumed the efficiency ϵ_{halo} to be a constant. However, since dwarf galaxies have stronger winds, lower metallicities and less dust than galaxies like our own, it is plausible that radiative losses during the thermalisation of ejecta energy are substantially smaller in dwarfs than in giants. We have therefore allowed for this possibility explicitly by setting

$$\epsilon_{\text{halo}} = \eta \times \left[0.5 + \left(\frac{V_{\text{max}}}{70\text{km/s}} \right)^{-\beta_2} \right], \quad (21)$$

where η is a free parameter which encodes possible variations about our IMF and SN assumptions, possible energy input from the winds and UV radiation of massive stars, and the radiative losses during ejecta thermalisation, while β_2 describes the dependence of this last factor on V_{max} . Again, we adjust these parameters when fitting to observations of the stellar mass function and gas-to-star ratios of galaxies. Our standard model below adopts $\eta = 0.32$ and $\beta_2 = 3.5$. We expect that $\epsilon_{\text{halo}} < 1$ and, unlike DLB07 or Bower et al. (2006), we enforce this constraint in all our models.

Given this energy input into disk and halo gas, the total amount of material that can be ejected from a halo/subhalo can be estimated as

$$\delta M_{\text{ejec}} = \frac{\delta E_{\text{SN}} - \frac{1}{2} \delta M_{\text{reheat}} V_{\text{vir}}^2}{\frac{1}{2} V_{\text{vir}}^2}. \quad (22)$$

If this equation gives $\delta M_{\text{ejec}} < 0$, we assume that the mass of reheated gas saturates at $\delta M_{\text{reheat}} = \delta E_{\text{SN}} / (\frac{1}{2} V_{\text{vir}}^2)$ and that no gas is ejected from the halo/subhalo.

The reheating and ejection efficiencies, ϵ_{disk} and ϵ_{halo} , decline with increasing halo circular velocity, saturating at 0.5ϵ and 0.5η , respectively. This dependence is controlled by the values of β_1 and β_2 which are chosen to fit the abundance of low-mass galaxies. β_1 primarily affects the low-mass slope of the stellar mass function, while β_2 affects its amplitude. Our default model has a very strong V_{max} -dependence, $\beta_1 = \beta_2 = 3.5$, but because of saturation effects the results are not very sensitive to this choice. For example, the adoption of $\beta_1 = \beta_2 = 1.5$ predicts a stellar mass function only slightly steeper than our default model and overpredicts the abundance of galaxies of stellar mass $10^8 M_{\odot}$ by 0.1 dex compared to the default model. This dependence of SN feedback on V_{max} also affects the metallicities of low-mass galaxies (see details in Sec. 4.3). Compared to DLB07, our model gives stronger feedback at low circular velocities. This is the primary reason that it produces fewer dwarf galaxies and that these have lower metallicities than in the earlier model.

The gas mass M_{ejec} thrown out of a system by these effects is stored in an ejecta ‘‘reservoir’’ associated with the halo/subhalo, whence it may later be reincorporated into the hot halo gas and so again become available for cooling onto the central galaxy. In low-mass halos, hot winds are likely to leave at a substantially higher velocity relative to the escape velocity and so their gas is likely to be more difficult to reaccrete. To allow for this possibility, we introduce a dependence of the reaccretion rate on halo/subhalo virial velocity,

$$\dot{M}_{\text{ejec}} = -\gamma \left(\frac{V_{\text{vir}}}{220\text{km/s}} \right) \left(\frac{M_{\text{ejec}}}{t_{\text{dyn,h}}} \right), \quad (23)$$

where γ is a free parameter which we take to be 0.3. With these choices, ejected gas is returned to the hot halo component in a few dynamical times for galaxies like the Milky Way, but takes substantially longer in dwarf systems.

The association of hot gaseous halos and ejecta reservoirs with satellite subhalos is a substantial change in our model with respect to DLB07. As detailed in the next subsection we explicitly model the stripping of these components by tidal and ram-pressure effects.

3.6 Satellite Galaxies in Groups and Clusters

In the following, we classify galaxies into three types according to their relationship to the dark matter distribution. Type 0 galaxies are the central galaxies of main subhalos and so can be considered as the principal galaxies of their FOF groups. Type 1 (satellite) galaxies lie at the centre of non-dominant subhalos, while type 2 (satellite) galaxies are those which no longer have an associated dark matter subhalo which is resolved by the simulation. The latter are often referred to as ‘‘orphan galaxies’’. All galaxies are born as type 0. They usually become type 1 when they fall into a group or cluster, and they may later become type 2. Type 2’s may later merge into the central galaxy of their halo.

FOF halos often link together two (or more) essentially disjoint dark matter structures, joining them with low-density ‘‘bridges’’ of particles. In such a situation, one would expect the central galaxies of the various objects to evolve independently until the smaller ones actually fall into the main body of the system. To represent this we have changed the treatment of type 1 galaxies from that in DLB07. When a type 0 galaxy first becomes type 1 (i.e. its FOF halo is first linked to a more massive FOF halo) we continue to treat it as a type 0 galaxy (i.e. in the same manner as a galaxy at the centre of a main subhalo) until it falls within R_{vir} of the centre of its new FOF halo. At this point we switch on tidal and ram-pressure stripping processes which can remove gas from the galaxy or even disrupt it completely. In our model such processes *only* occur within R_{vir} so that if a satellite passes outside R_{vir} again it is once more treated in the same way as a type 0 galaxy.² This change primarily affects galaxies between R_{vir} and the boundary of the FOF group. It leads to a reduction in the number of ‘‘true’’ satellite galaxies (e.g. galaxies whose evolution is influenced by being a non-central object within a larger system). We discuss the number of galaxies affected by this change, as well as the overall number of satellites and of orphans in our MS and MS-II models, in Appendix A.

² Since only the main subhalo of a FOF halo has an associated R_{vir} , this quantity is not available for ‘‘independent’’ type 1 galaxies outside the R_{vir} of their new FOF halo. For such objects we use the values of R_{vir} and M_{vir} recorded at the last time they were type 0’s when values of these quantities are required in our cooling recipe.

3.6.1 Gas Stripping

In most semi-analytic models, hot gas associated with a halo is assumed to be stripped immediately after accretion onto a larger system, leading to a rapid decline in star formation and a reddening in colour (e.g. Wang et al. 2007; Weinmann et al. 2006; Baldry et al. 2006; Font et al. 2008). In the real Universe (Sun et al. 2007; Jeltama et al. 2008) and in hydrodynamic simulations, however, the hot atmosphere of massive satellite galaxies may survive for some considerable time after accretion. McCarthy et al. (2008) found that for satellite galaxies with typical structural and orbital parameters, up to 30% of the initial hot halo gas can remain in place for up to 10 Gyr. Weinmann et al. (2009) and Font et al. (2008) constructed MS-based models for incremental, rather than instantaneous removal of material through tidal stripping and ram-pressure stripping. In the following we describe how we include both mechanisms in our own models, which are similar to but different in detail from those of Weinmann et al. (2009) and Font et al. (2008).

We assume the hot gas in a subhalo to have a distribution that exactly parallels that of the dark matter. Since tidal acceleration acts identically on hot gas and dark matter at each location, we take the hot gas mass to be reduced by tidal stripping in direct proportion to the subhalo’s dark matter mass. The latter is, of course, followed explicitly in a dynamically consistent way by the original simulation. Thus we assume

$$\frac{M_{\text{hot}}(R_{\text{tidal}})}{M_{\text{hot,infal}}}} = \frac{M_{\text{DM}}}{M_{\text{DM,infal}}}, \quad (24)$$

where $M_{\text{DM,infal}}$ and $M_{\text{hot,infal}}$ were the DM mass of the subhalo and the mass of its associated hot gas when its central galaxy was last a type 0, and M_{DM} and M_{hot} are the current masses of these two components. Recall that we assume $\rho \propto r^{-2}$ for the hot gas distribution, thus $M_{\text{hot}}(r) \propto r$. The tidal radius beyond which the hot gas is stripped can be thus expressed as

$$R_{\text{tidal}} = \left(\frac{M_{\text{DM}}}{M_{\text{DM,infal}}} \right) R_{\text{DM,infal}} \quad (25)$$

where $R_{\text{DM,infal}}$ was the virial radius of the subhalo just before it became a satellite.

In addition to tidal forces, the hot gas around satellite galaxies experiences ram-pressure forces due to satellite’s motion through the intracluster medium (ICM). At a certain distance, $R_{\text{r.p.}}$, from the centre of the satellite, self-gravity is approximately balanced by this ram pressure:

$$\rho_{\text{sat}}(R_{\text{r.p.}}) V_{\text{sat}}^2 = \rho_{\text{par}}(R) V_{\text{orbit}}^2, \quad (26)$$

where $\rho_{\text{sat}}(R_{\text{r.p.}})$ is the hot gas density of the satellite at radius $R_{\text{r.p.}}$, V_{sat} is the virial velocity of the subhalo at infall (which we assume to be constant as the subhalo orbits around the main halo), $\rho_{\text{par}}(R)$ is the hot gas density of the parent dark matter halo at distance R from the centre of its potential well, and V_{orbit} is the orbital velocity of the satellite, which we estimate as the virial circular velocity of the main halo. The ram-pressure dominates over gravity beyond $R_{\text{r.p.}}$ and hot gas at these radii is stripped.

We compare the two radii R_{tidal} and $R_{\text{r.p.}}$ and define the minimum of the two as the stripping radius

$$R_{\text{strip}} = \min(R_{\text{tidal}}, R_{\text{r.p.}}). \quad (27)$$

Beyond R_{strip} , we assume all the hot gas to be removed without modifying the gas profile within R_{strip} . Thus the cooling rate onto the centre is not affected, to lowest order, by this stripping. We assume gas in the “ejecta reservoir” of a subhalo to be stripped in proportion to the hot gas. It is unclear where this reservoir should be located and whether or not it will be affected by ram-pressure effects (e.g. whether it is primarily diffuse or in relatively dense clouds). Thus we adopt the simple approach of stripping it in proportion to the hot gas. Stripped material from each of these components is added to the corresponding component associated with the central (type 0) galaxy of the main subhalo, and so can never fall back onto its original subhalo.

In addition to stripping, at least two other processes affect the hot gas halos of satellites. One is cooling. The hot gas in satellite galaxies can cool onto the central cold star-forming disk. We assume that the temperature of the hot gas atmosphere is not changed by stripping and cooling processes, remaining pegged to its value at infall. The cooling rate is calculated just as in Sec. 3.2, which ensures continuity in cooling rates as central galaxies turn into satellite galaxies. As cooling depletes the hot atmosphere, we assume its density to drop everywhere, but its profile shape and bounding radius to remain the same.

SN feedback also modifies the hot atmospheres and ejecta reservoirs of satellite galaxies. As in central galaxies, star formation in satellites releases large amounts of energy, reheating both cold ISM gas and the hot gas atmosphere. Font et al. (2008) presented a model in which both the hot and the reheated gas of satellites is stripped primarily in the initial infall event. They found that the satellite galaxy properties are very sensitive to the way the secondary reheated gas (which is only reheated after the galaxy has become a satellite) is stripped. If it is stripped as in the initial infall event, satellite galaxies lose all gas and become red very rapidly. In order to retain gas and keep satellites blue for longer, they adopted a stripping efficiency for this secondary reheated gas which is only 10% of that at infall, and they do not strip any of the hot gas after the initial stripping event. In our model, we have adopted continuous stripping, in which hot and ejected components are stripped equally at each timestep as long as the galaxy is a satellite. We assume the reheated gas to extend to a radius equal to the virial radius of the subhalo at infall. Taking into account the stripping mechanisms discussed above, only reheated gas within R_{strip} (i.e. a fraction $R_{\text{strip}}/R_{\text{DM,infal}}$ of the total reheated gas) remains in the subhalo; the rest is added to the hot atmosphere of the main halo. If SN is strong enough to predict that material should be ejected from the subhalo altogether, then we use the formulae given above for central galaxies (Equations (20) and (22)), and distribute the ejected material between the ejecta reservoirs of the satellite and central galaxies in the same proportions as the reheated gas. In general, the stripping of gas in our model is more efficient than in Font et al. (2008), but considerably less efficient than in DLB07.

Our current model differs from that of DLB07 both because galaxies effectively become satellites later (when they cross R_{vir} rather than when they become part of a larger FOF group) and because satellites retain their hot gas components and ejecta reservoirs until these are removed by stripping (rather than losing them as soon as they become

satellites). Satellites thus retain more fuel for star formation and can be expected to stay blue longer. Note that ram-pressure stripping does not affect the cold gas component of galaxies in our models. This is unrealistic for galaxies in the inner regions of rich clusters and results in passive S0 galaxies retaining significant gas and dust which should probably have been removed (see Fig. 11).

We illustrate the effect of our modification of stripping recipes in Fig. 3. We select 1000 galaxy clusters from the MS with $M_{\text{vir}} > 2 \times 10^{14} M_{\odot}$. For each, we calculate the fraction of actively star-forming galaxies as a function of projected distance from the centre in units of R_{vir} , and we average over all clusters. ‘‘Actively star-forming’’ here means having a specific star formation rate (SSFR, the ratio of star formation rate to stellar mass) above 10^{-11}yr^{-1} . We consider galaxies with velocity relative to cluster centre (peculiar + $H_0 \times$ line-of-sight distance difference) less than $3 \times V_{\text{vir}}$, dividing them into four stellar mass bins as indicated by the $\log M_*$ ranges given in the bottom right corner of each panel. To emphasize the environmental effects which concern us here, each active galaxy fraction is normalized to its ‘‘field’’ value, estimated at $20R_{\text{vir}}$. Symbols with error bars are observational data from Weinmann et al. (2009) based on the SDSS cluster sample of von der Linden et al. (2007). Predictions from our model are in red, those from the model of DLB07 in black. Clearly, within R_{vir} , the changes we have introduced do slow the decline of star formation in satellite galaxies, although the differences are not large. This is because satellites start to be stripped later in our new recipes, and even thereafter they retain some hot gas which can fuel star formation and keep them blue, whereas in DLB07, hot gas is stripped immediately once galaxies become attached to a larger FOF group and star formation ceases once their cold ISM gas is used up. Note, however, that the fraction of active galaxies in the field differs between our model and DLB07, with our model predicting somewhat lower active fractions in general, thereby worsening the overall agreement with observation. This is a result of the enhanced feedback we have introduced in order to match the observed stellar mass function (see Sec 3.9).

3.6.2 Disruption

The stellar component in subhalos can also be stripped in the presence of very strong tidal forces. Usually, the galaxy is harder to disrupt than its dark halo because it is more compact and denser. We thus assume that the stellar component of a satellite galaxy is affected by tidal forces only after its subhalo has been entirely disrupted, i.e. it has become a type 2 galaxy. The position of such a galaxy is identified with that of the most bound particle of its subhalo at the last time the subhalo could be identified. To estimate when stripping of stars is important we assume the satellite orbits in a singular isothermal potential,

$$\phi(R) = V_{\text{vir}}^2 \ln R. \quad (28)$$

Assuming conservation of energy and angular momentum along the orbit, its pericentric distance can be estimated from:

$$\left(\frac{R}{R_{\text{peri}}} \right)^2 = \frac{\ln R/R_{\text{peri}} + \frac{1}{2} (V/V_{\text{vir}})^2}{\frac{1}{2} (V_t/V_{\text{vir}})^2}, \quad (29)$$

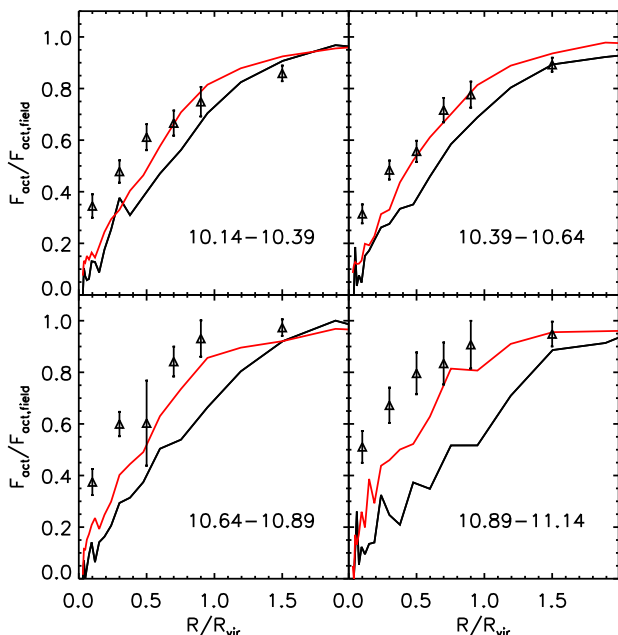


Figure 3. The reduction in the fraction of actively star-forming galaxies ($\dot{M}_*/M_* > 10^{-11} \text{yr}^{-1}$) as a function of projected distance from cluster centre in units of R_{vir} . The four panels refer to different ranges of $\log M_*/M_{\odot}$ as indicated by the labels. Predictions from the preferred model of this paper applied to the MS are shown in red, those from the model of DLB07 in black. Symbols with error bars are SDSS data for a large sample of nearby clusters taken from Weinmann et al. (2009). For each curve the fraction of actively star-forming galaxies is normalised by its ‘‘field’’ value, taken to be the value at $20 R_{\text{vir}}$. This emphasises the effect of cluster environment on star formation activity.

where R is the current distance of the satellite from halo centre, and V and V_t are the velocity of the satellite galaxy with respect to halo centre and its tangential part, respectively.

We compare the main halo density at pericentre with the average baryon mass (cold gas mass + stellar mass) density of satellite within its half mass radius. If

$$\frac{M_{\text{DM,halo}}(R_{\text{peri}})}{R_{\text{peri}}^3} \equiv \rho_{\text{DM,halo}} > \rho_{\text{sat}} \equiv \frac{M_{\text{sat}}}{R_{\text{sat,half}}^3}, \quad (30)$$

we assume the satellite galaxy is disrupted entirely. Its stars are then assigned to a population of intracluster stars (ICS) and its cold gas and the associated metals are added to the hot gas atmosphere of the halo central galaxy. Note that this calculation does not fully account for dynamical friction effects on the satellite orbit, which are underestimated by the simulation once the remaining mass of a subhalo drops below the stellar mass of its associated galaxy. Note also that we do not model continuous disruption. Rather, once Equ. (30) is satisfied, satellite galaxies are disrupted completely. When a central type 0 galaxy merges in to a larger system and becomes a type 1 satellite, it carries its ICS with it until it becomes a type 2 galaxy. At this point, its current central galaxy acquires its ICS.

3.7 Mergers

Mergers can occur between a central galaxy and a satellite galaxy, and between two satellite galaxies. In the MS, the minimum resolved subhalo has a mass of $2.3 \times 10^{10} M_{\odot}$. The stellar mass of the galaxy within a given subhalo is thus smaller than the subhalo mass, except in the case of very massive satellites. In the MS-II, however, the minimum subhalo mass is $1.9 \times 10^8 M_{\odot}$, and the stellar mass of a galaxy often becomes larger than the mass of its host subhalo well before we lose the track of the subhalo. In this situation the simulation no longer correctly follows the expected decay of the satellite orbit through dynamical friction. In this paper we therefore modify the DLB07 treatment of mergers, which estimated a dynamical friction time until merging only once the satellite’s subhalo is fully disrupted. Here we estimate this decay time as soon as the mass of a subhalo drops below that of the galaxy it contains, and we immediately set the countdown clock for merging. The position and velocity of the satellite galaxy are thereafter traced by the most bound particle of the subhalo at the time the merger clock was switched on, modified by a time-dependent orbit-shrinking factor which models the orbital decay caused by the dynamical friction (see below). As in DLB07, we adopt the dynamical friction formula of Binney & Tremaine (1987) to estimate the merging time for a satellite galaxy,

$$t_{\text{friction}} = \alpha_{\text{fric}} \frac{V_{\text{vir}} r_{\text{sat}}^2}{G m_{\text{sat}} \ln \Lambda}. \quad (31)$$

where $\alpha_{\text{fric}} = 2.34$. DLB07 found this coefficient to be needed to reproduce observed luminosity functions at the luminous end. It was also found to be appropriate in the N-body studies of Boylan-Kolchin et al. (2008) and Jiang et al. (2008). Unlike DLB07, we here take m_{sat} to be the sum of the baryonic mass of the satellite galaxy and the dark matter mass of its subhalo. The dark matter mass here refers to the mass of the subhalo just before the merger clock is set. r_{sat} is the distance between the central and satellite galaxies at the time when we start the merger clock, and $\ln \Lambda = \ln(1 + M_{\text{vir}}/m_{\text{sat}})$ is the Coulomb logarithm. After a time t_{friction} the satellite galaxy is assumed to merge with the central galaxy of the main halo. If a main halo is accreted onto a larger system and becomes a subhalo, any of its satellites for which the merger clock is already set are assumed to keep orbiting within this subhalo and to merge into its central galaxy when the time runs out. In this way, our model allows satellites to merge into the central galaxies of both main and subdominant subhalos (although the latter is quite rare).

We have also attempted to model approximately the dynamical friction driven orbital decay of type 2 galaxies which leads to their eventual merging with the central galaxy, even though the low-mass subhalo or the simulation particle with which the galaxy is associated clearly experiences no such decay. A simple model in which an “isothermal” satellite spirals to the centre of a larger “isothermal” host on a near circular orbit predicts that the radius of the orbit should decay linearly in time. To mimic this, we multiply the positional offset of the tracer particle from the central galaxy with which its galaxy is destined to merge by a factor $(1 - \Delta t/t_{\text{friction}})$ to define the position of the galaxy, where Δt is the time since the merger clock was initialised. The

velocity of the galaxy is kept equal to that of the tracer particle.

Our modelling differentiates between major and minor mergers. Major mergers are those between galaxies with baryonic masses differing by less than a factor of three. More extreme mass ratios are treated as minor mergers. During a major merger, the disks of the progenitors are destroyed completely, leading to the formation of a spheroidal remnant. In a minor merger, the disk of the larger progenitor survives and accretes the cold gas and stellar components of the small galaxy. In both cases, the merger triggers a starburst which we represent using the “collisional starburst” model of Somerville et al. (2001). During the merger, a fraction, e_{burst} , of the cold gas of the merging galaxies is converted into stars, where

$$e_{\text{burst}} = 0.56 \left(\frac{M_{\text{minor}}}{M_{\text{major}}} \right)^{0.7}, \quad (32)$$

and M_{minor} and M_{major} are the total baryon masses of the minor and major progenitors, respectively. The coefficient and index here are consistent with those given by Cox et al. (2008) and Somerville et al. (2008). The stars formed during major mergers contribute to the elliptical remnants, while those formed during minor mergers are added to the disks. Feedback and chemical enrichment from the starburst are modeled in the same way as for quiescent star formation, and the strong SN feedback produced by a major merger can expel almost all the remaining cold gas from the system, suppressing further star formation until a new gas disk grows.

To summarize, our treatment of mergers differs from that of DLB07 only in that we switch on the merger clock as soon as the dark matter mass of a subhalo drops below the baryonic mass of its central galaxy, that we take into account the baryonic mass of the galaxy when calculating the dynamical friction time, and that we include an approximate representation of the shrinkage of orbits caused by dynamical friction. Many aspects of these recipes are quite crude but they nevertheless represent reasonably well the results of recent simulations of both gas-poor and gas-rich galaxy mergers (e.g. Naab & Burkert 2003; Cox et al. 2008).

3.8 Bulge Formation

Three modes of bulge growth are included in our model: major mergers, minor mergers and disk buckling.

After a major merger, all stars from the progenitors and all the newly formed stars are assumed to end up in a spheroidal component. After a minor merger, the disk of the larger progenitor remains intact but its bulge acquires all the pre-existing stars from the minor progenitor, while the newly formed stars are added to the disk. In both cases, the spheroidal component grows in mass and changes in size. We use energy conservation and the virial theorem to estimate the change in size:

$$C \frac{GM_{\text{new,bulge}}^2}{R_{\text{new,bulge}}} = C \frac{GM_1^2}{R_1} + C \frac{GM_2^2}{R_2} + \alpha_{\text{inter}} \frac{GM_1 M_2}{R_1 + R_2}, \quad (33)$$

where C is a structure parameter relating the binding energy of a galaxy to its mass and radius, and α_{inter} is a parameter quantifying the effective interaction energy deposited in

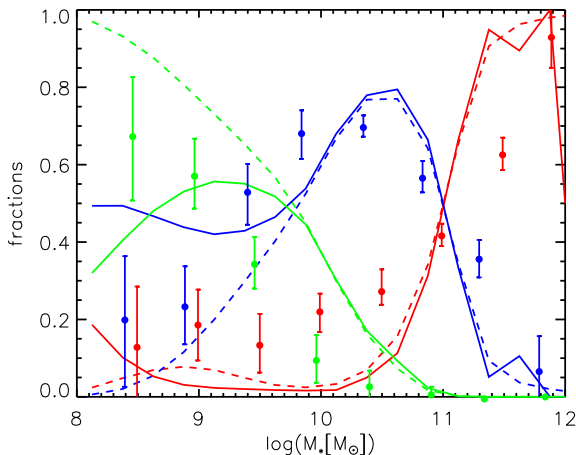


Figure 4. The distribution of galaxies across morphological type as a function of stellar mass. Red lines show the fraction of galaxies with $\frac{M_{\text{bulge}}}{M_{\text{total}}} > 0.7$, which we consider to represent elliptical galaxies. Blue lines indicate galaxies with $0.03 < \frac{M_{\text{bulge}}}{M_{\text{total}}} < 0.7$ (normal spirals) and green indicate $\frac{M_{\text{bulge}}}{M_{\text{total}}} < 0.03$, essentially pure-disk or extreme late-type galaxies. Model results for the MS are shown with dashed lines and for the MS-II with solid lines. The symbols give observational results for real galaxies from Conzelmann (2006).

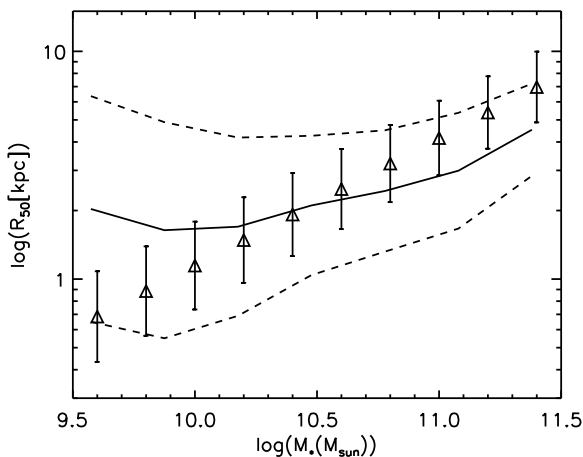


Figure 5. Half-mass radius as a function of stellar mass for early-type galaxies, which we define as galaxies with SDSS concentration parameter $c > 2.86$. The solid curve gives the median half-mass radius predicted by our model at each stellar mass, while dashed curves show the *rms* scatter in $\log R$. Symbols with error bars indicate the median and *rms* scatter of observational estimates taken from the SDSS study of Shen et al. (2003).

the stellar components. $C = 0.49$ for an exponential disk whereas $C = 0.45$ for a bulge with an $r^{1/4}$ profile; to simplify, we adopt $C = 0.5$. We also set $\alpha_{\text{inter}} = 0.5$, so that $\alpha_{\text{inter}}/C = 1$. This is roughly consistent with the numerical simulation results of Boylan-Kolchin et al. (2005) which give $1.3 < \alpha_{\text{inter}}/C < 1.7$ for the most probable orbits of dissi-

tionless major mergers of elliptical galaxies. We prefer a slightly smaller value of α_{inter} because it gives bulge sizes in better agreement with observation (see below). A similar formula was used by Cole et al. (2000), but rather than following subhalo mass directly, as in our approach, they used analytic formulae to estimate the dark matter mass of satellites just prior to merging. This dark matter mass was included in their analogue of Equ. 33. In our model, the dark matter mass of satellites is almost always very small (or zero) at the time they merge. Further, we assume the final merger to be from a tightly bound orbit. Thus we neglect the effects of dark matter and use the stellar masses of the two objects in Equ. 33.

The term on the left-hand side of Equ. (33) is the binding energy of the final bulge: $M_{\text{new,bulge}}$ is its stellar mass and $R_{\text{new,bulge}}$ is its half-stellar-mass radius. The first and second terms on the right-hand side are the self-binding energies of the two individual progenitors, while the third term is the binding energy invested in their orbit at merger. For major mergers, M_1 and M_2 are the sum of the mass of stars and of the cold gas converted into stars for the two progenitors, and R_1 and R_2 are the corresponding half mass radii. For minor mergers, M_1 and R_1 are the mass and half-mass radius of the bulge of the major progenitor, and M_2 and R_2 are the stellar mass and the half-stellar-mass radius of the minor progenitor.

Secular evolution is thought to be another important channel for the formation of galaxy bulges, in particular in systems where the self-gravity of the disk is dominant. Here we adopt the same simple, schematic criterion as DLB07 to delineate disk instability:

$$V_{\text{max}} < \sqrt{\frac{GM_{*,\text{d}}}{3R_{*,\text{d}}}} \quad (34)$$

where $M_{*,\text{d}}$ and $R_{*,\text{d}}$ are the stellar mass and exponential scale length of the stellar disk, and V_{max} , as usual, is the maximum circular velocity of the DM (sub)halo hosting the disk. In the original presentation of this criterion by Efstathiou et al. (1982) the factor of 3 was missing and V_{max} represented the maximum circular velocity of the combined disk-halo system. The smaller coefficient used here reflects the facts that this latter V_{max} is expected to be significantly larger than the maximum circular velocity of the unperturbed dark halo for realistic systems near the instability boundary, and that more recent simulations have shown exponential disks in NFW halos to be somewhat more stable than would be inferred from the early experiments of Efstathiou et al. (1982) (see, for example, Sellwood & Moore 1999; Sellwood & Evans 2001).

When the criterion of Equ. (34) is met, we transfer mass, δM_* , from the disk to the bulge to keep the disk marginally stable. Recall that we assume an exponential density profile for the stellar disk. Here we further assume that the mass is transferred from the inner part of the disk and that the bulge formed in this way occupies the corresponding region (i.e. the bulge half-mass radius equals to the radius of this region):

$$\delta M_* = 2\pi \Sigma_{*,\text{d}} R_{*,\text{d}} [R_{*,\text{d}} - (R_{\text{b}} + R_{*,\text{d}}) \exp(-R_{\text{b}}/R_{*,\text{d}})], \quad (35)$$

where R_{b} is the half-mass radius of the newly formed bulge, and covers the region from which the stellar mass is transferred into the bulge. We assume that negligible angular

momentum is transferred to the bulge from the disk with these stars so that the angular momentum of the disk is unchanged. Since we also assume an unchanged rotation velocity and an exponential profile, the disk exponential scale length increases and its central surface density decreases when stars are transferred to the bulge.

If there is already a bulge present when a disk goes unstable, we assume the instability to produce a new bulge with half mass radius R_b given by Equ. (35), which “merges” into the existing bulge in the same way as in galaxy mergers, simply replacing M_1 and R_1 with the mass and half-mass radius of the existing bulge, and replacing M_2 and R_2 with δM_* and R_b . The only difference is that we set $\alpha_{\text{inter}} = 2$ in this case, since the interaction energy between the “old” and “new” bulges is stronger than in the case of galaxy mergers since the two are concentric.

To illustrate how well these recipes work, Fig. 4 compares observational data to model predictions for the distribution of galaxies across morphological type as a function of stellar mass. Red curves are for galaxies with $M_{\text{Bulge}}/M_{\text{total}} \geq 0.7$ (“elliptical galaxies”), blue for galaxies with $0.7 > M_{\text{Bulge}}/M_{\text{total}} \geq 0.03$ (“normal spirals”) and green for galaxies with $M_{\text{Bulge}}/M_{\text{total}} < 0.03$ (“pure disks”). Solid and dashed curves are results based on the MS-II and the MS, respectively. The two simulations produce convergent results above $\log M_* = 10$, but they differ progressively at lower stellar masses because the resolution of the MS is no longer good enough to follow accurately the detailed formation histories of the galaxies. The symbols in Fig. 4 are observational results from Conselice (2006). These agree well with the models, provided the MS-II results are taken at low stellar masses. To study the relative roles in of disk instability and mergers in building bulges, we calculated a model without the disk instability mode. This showed that in our default model, disk instability is a major contributor to bulge formation in intermediate mass galaxies like the Milky Way. At both higher and lower masses, mergers are the dominant mechanism; in particular, massive elliptical galaxies are built by mergers. This is consistent with the results found by De Lucia et al. (2006) using our previous galaxy formation model.

To illustrate how well our simple recipe reproduces the sizes of the spheroidal components of galaxies, Fig. 5 plots half-mass radius against stellar mass for early-type galaxies defined to be those with concentration parameter $c > 2.86$ (see 3.3 for how we estimate c ; in practice, this limit corresponds approximately to $M_{\text{Bulge}}/M_{\text{total}} > 0.20$). A solid curve gives our model prediction for the median half-mass radius at each stellar mass, while dashed curves indicate the predicted scatter. The symbols are SDSS results for the median and scatter from Shen et al. (2003). Overall, agreement is fair, at best. At lower masses, our default model predicts a larger median value than is observed, perhaps reflecting gas dissipation during gas-rich mergers (e.g. Hopkins et al. 2009). Indeed, recent work suggests that including gas dissipation may explain both the steep slope of the size vs. stellar mass relation (Dekel & Cox 2006), and its small scatter (Covington et al. 2008). It is also noticeable that the scatter in size is larger in our simple model than in the SDSS data, particularly at low mass. These deficiencies actually become worse if we restrict the sample to more strongly bulge-dominated galaxies, since a significant part

of the trend in this figure is due to the size-stellar mass relation for disks highlighted in Fig. 2. The small observed scatter has recently been confirmed for a large sample of visually classified SDSS galaxies by Nair et al. (2010) who emphasise that a tight relation may be difficult to understand if spheroids are built stochastically through mergers. Our model confirms that this may be a problem and that a more detailed theoretical treatment is warranted.

3.9 Black Hole Growth and AGN feedback

There is growing evidence that galactic nuclear activity is closely related to galaxy formation. Here we follow Croton et al. (2006), separating black hole growth into two modes: “quasar” mode and “radio” mode.

The quasar mode applies to black hole growth during gas-rich mergers. During a merger, the central black hole of the major progenitor grows both by absorbing the central black hole of the minor progenitor, and by accreting cold gas. The total growth in mass is calculated as

$$\delta M_{\text{BH}} = M_{\text{BH},\text{min}} + f \left(\frac{M_{\text{min}}}{M_{\text{maj}}} \right) \left(\frac{M_{\text{cold}}}{1 + (280\text{km/s}/V_{\text{vir}})^2} \right), \quad (36)$$

where $M_{\text{BH},\text{min}}$ is the mass of the black hole in the minor progenitor, M_{cold} is the total cold gas in the two progenitors, and M_{min} and M_{maj} are the total baryon masses of the minor and major progenitors, respectively. Here f is a free parameter, which, following Croton et al. (2006) we set to 0.03 in order to reproduce the observed local $M_{\text{BH}} - M_{\text{bulge}}$ relation. Both major mergers and gas-rich minor mergers contribute significantly to the growth of the black hole. We do not explicitly model feedback due to this mode, which always coincides with a starburst in the merging galaxies. Any feedback from accretion onto the black holes can be thought of as being part of the substantial energy input which we assume this starburst to produce. As noted above, this is often sufficient to eject all the gas from the merger remnant.

Radio mode growth occurs through hot gas accretion onto central black holes. The growth rate in this mode is calculated, following Croton et al. (2006), as

$$\dot{M}_{\text{BH}} = \kappa \left(\frac{f_{\text{hot}}}{0.1} \right) \left(\frac{V_{\text{vir}}}{200\text{km s}^{-1}} \right)^3 \left(\frac{M_{\text{BH}}}{10^8/hM_{\odot}} \right) M_{\odot}/\text{yr}, \quad (37)$$

where, for a main subhalo, the hot gas fraction, f_{hot} , is the ratio of hot gas mass, M_{hot} , to subhalo dark matter mass M_{DM} , while for a type 1 galaxy in a satellite subhalo, f_{hot} is the ratio of hot gas mass to dark matter mass within R_{strip} , $\frac{R_{\text{strip}}}{R_{\text{DM},\text{infall}}} M_{\text{DM},\text{infall}}$. The parameter κ sets the efficiency of hot gas accretion. Again following Croton et al. (2006), we assume that this hot mode accretion deposits energy in relativistic jets with 10% efficiency and that this energy is then deposited as heat in the hot gas atmosphere, as is observed directly through radio bubbles in galaxy clusters (e.g. McNamara & Nulsen 2007; Bîrzan et al. 2004). Specifically, we assume an energy input rate:

$$\dot{E}_{\text{radio}} = 0.1 \dot{M}_{\text{BH}} c^2, \quad (38)$$

where c is the speed of light. The effective (net) mass cooling rate is thus

$$\dot{M}_{\text{cool,eff}} = \dot{M}_{\text{cool}} - 2\dot{E}_{\text{radio}}/V_{\text{vir}}^2. \quad (39)$$

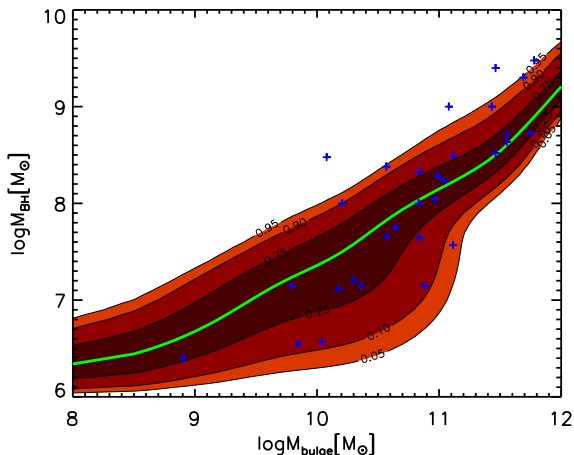


Figure 6. The relation between black hole mass and bulge stellar mass at $z = 0$. Red contours give predictions from our model applied to the MS-II. The distributions in black hole mass are normalised to unity at each stellar mass and the contours indicate their 5, 10, 25, 75, 90 and 95 percentage points. The green curve represents the median values. Blue crosses are observational data taken from Häring & Rix (2004).

Note this specific form of “radio mode feedback” is only one possible description of AGN feedback, and other forms can give quite similar results (e.g. Bower et al. 2006). Moreover, there is no direct observational evidence that radio mode feedback can offset cooling in halos with mass as low as $\sim 10^{13} M_{\odot}$, where it plays an important role in our models.

In our preferred model the accretion efficiency κ is set to be 1.5×10^{-5} in order to match the high-mass end of the stellar mass function. This is twice the value adopted in DLB07 ($\kappa = 7.5 \times 10^{-6}$). There are three reasons for this change, in addition to the fact that the new SDSS stellar mass functions cut off at high mass more strongly than the data used in DLB07. The first is that DLB07 assumed the hot gas mass of a halo to be $f_b^{\text{cos}} M_{\text{vir}}$ minus the baryonic masses of all the galaxies associated with the FOF group, even those which lie outside R_{vir} . Here we subtract only the baryonic masses of the galaxies that lie inside R_{vir} , resulting in higher estimates of M_{hot} and so larger cooling rates which the radio mode feedback must offset. The second reason is that we have introduced a “disruption” mechanism which destroys some type 2 galaxies which previously survived in galaxy clusters. The ISM of these disrupted galaxies adds additional metal-rich material to the hot gas atmosphere, again enhancing its predicted cooling rate relative to the previous model. The final reason is that the enhanced feedback at low mass, which we have introduced in order to match the observed $z = 0$ stellar mass function, results in more gas remaining available to cool at later times. Note that our model assumes the hot gas in all systems to be distributed with $\rho \propto r^{-2}$ at the virial temperature T_{vir} . In reality, feedback both from star formation and from an AGN may well change the profile of the surrounding hot gas, making it less centrally concentrated and less able to cool. This would result in less need for feedback at later times. (See Bower et al. (2008) for a simple model based on this idea.) As may be

seen in Fig. 6, the increased feedback efficiency in our new model does not significantly affect its fit to the observed relation between the black hole mass and bulge stellar mass. This is because black hole growth is in any case dominated by the quasar mode.

Radio mode feedback works in essentially the same way in our model as in Croton et al. (2006) and DLB07. It is more effective at low redshift and in massive objects, both because the black hole is more massive, and because the hot gas fraction is higher there. The effect has a very weak, if any, dependence on large-scale environment (Croton & Farrar 2008). Note that our model differs from DLB07 in that radio mode can also operate in satellite galaxies at the centres of their own subhalos. In DLB07, such satellite subhalos no longer retained any hot gas so that radio mode activity was completely quenched there.

3.10 Metal Enrichment

Our treatment of metal enrichment follows that of De Lucia et al. (2004) quite closely. Here we briefly summarise the various processes we include. As stars evolve, both heavy elements and a fraction of the initial stellar mass are returned instantaneously to the cold gas component of the ISM. The new material is assumed to be fully mixed with the pre-existing cold gas. A more realistic treatment should take into account the time delay between star formation and the return of both mass and metals to the interstellar medium. While the return of mass and metals from SN type II is indeed effectively instantaneous for the purposes of galaxy evolution, the same is not true for SN type Ia. In addition, mass loss and metal enrichment from intermediate mass stars takes place over Gyr timescales and is also important for a detailed understanding of metallicity patterns in galaxies. We intend to implement these processes in future work. In our current model, metals are carried into hot gas atmospheres and ejecta reservoirs when SN feedback reheats cold disk gas and ejects it. Metals from both these components can then be stripped from satellite galaxies and added to the corresponding components of the host system. Reincorporation and cooling can then take the metals into another (or the same) galaxy again. A more detailed description of metal enrichment and the exchange between different components can be found in De Lucia et al. (2004).

3.11 Stellar Population Synthesis and Dust Extinction

To compare model prediction with observations, we need to calculate the photometric properties of our model galaxies. Here we again follow DLB07, using stellar population synthesis models from Bruzual & Charlot (2003). We adopt a Chabrier initial function which has fewer low-mass stars than a Salpeter IMF and is a better fit to observational data both in our own Galaxy and in those nearby early-type galaxies for which detailed dynamical data are available (e.g. Cappellari et al. 2006). A detailed description can be found in De Lucia et al. (2004). We also follow DLB07 and adopt a slab dust model to account for the extinction of the star light. At higher redshift, we extend this model as in Guo & White (2009). Extinction is modeled as a function of gas column density, metallicity and redshift. The main difference

from DLB07, is that a redshift dependence is introduced so that for galaxies of given gas metallicity, the gas-to-dust ratio is higher at high redshift than in the local universe. This is motivated by observational data on high-redshift galaxies (e.g. Steidel et al. 2004; Quadri et al. 2008). Kitzbichler & White (2007) found that such a redshift dependence was needed for the DLB07 galaxy formation model to reproduce faint galaxy counts and redshift distributions, while Guo & White (2009) needed it to reproduce the abundance and clustering of colour-selected galaxy populations at redshifts of 2 and 3 (see these papers for details).

4 SYSTEMATIC PROPERTIES OF THE GALAXY POPULATION

In the last section we set out our new galaxy formation model and clarified the areas where it significantly alters or extends the earlier model of DLB07. Several of these extensions involve processes which were not previously included, notably the separate evolution of the sizes and orientations of gaseous and stellar disks, the size evolution of spheroids, tidal and ram-pressure stripping of satellite galaxies, and the disruption of galaxies to produce intracluster light. To illustrate the effects of these new ingredients, we have already presented a number of results from a simultaneous application of the new model to the MS and MS-II. In the current section we present a wide range of further results, primarily for the low-redshift universe where recent data now constrain the galaxy population over a range exceeding six orders of magnitude in stellar mass. By combining the MS and MS-II we are able to test our model against observation over this full range - the first time this has been possible using a direct simulation technique. By combining the two simulations we are also able to check explicitly how our results are affected by their limited mass resolution (as already done, for example, in Fig. 4).

We begin with a comparison of our model with the observed stellar mass function of galaxies, because we use this as the primary constraint on the various parameters in our star-formation and feedback models. We summarize these parameters and the values we assign to them in our preferred model in Table 1. Note that other model parameters (for example, those in our treatments of cooling, of disk and spheroid sizes, and of stripping, merging and disruption) also affect the stellar mass function, but we have set these to agree with other simulation or observational data, whereas the parameters in Table 1 were chosen primarily to fit the stellar mass function, and secondarily to ensure that gas-to-star ratios are in reasonable accord with observation. Because of the coupling between different parts of the model, an iterative method has to be used to find acceptable parameter sets. Those of our preferred model are almost certainly not unique, but they all lie within the physically plausible range discussed, for example, by Croton et al. (2006). Indeed, where the meanings correspond, our parameters are close to those presented in that paper and DLB07, except in a few cases which we highlight individually.

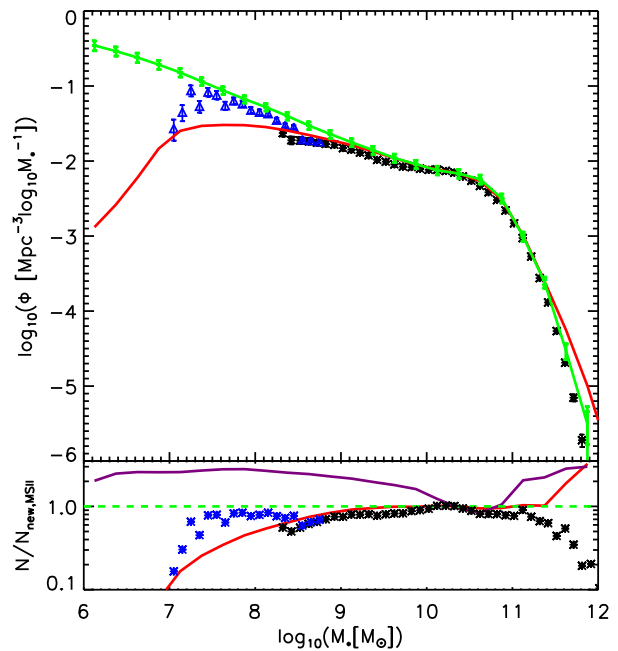


Figure 7. The abundance of galaxies as a function of their stellar mass. In the upper panel, green and red curves give the predictions of our preferred model when applied to the MS-II and the MS, respectively. The error bars on the MS-II curve show a “cosmic variance” uncertainty estimated from the *rms* scatter in the mass functions among 125 disjoint subvolumes of the MS, each with volume equal to that of the MS-II. Stars with error bars are the observational result, including cosmic variance uncertainties, for SDSS/DR7 as given by Li & White (2009) after a correction to total stellar masses following Guo et al. (2010). Blue triangles with error bars are the SDSS/DR4 results of Baldry et al. (2008). These are corrected for surface brightness incompleteness, but the error bars do not include cosmic variance uncertainties which are quite large for these low-mass objects. In the lower panel, black (Li & White 2009) and blue (Baldry et al. 2008) symbols show the abundance ratio of the SDSS data to our model prediction based on the MS-II. The red curve is the ratio of our MS and MS-II predictions, while the purple curve is the ratio of the DLB07 prediction to our MS-II prediction. A dashed green line indicates a ratio of unity.

4.1 Stellar Mass and Luminosity Functions

In Fig. 7 we compare the predictions of our preferred model to the observed abundance of galaxies as a function of stellar mass. The solid green curve is the prediction based on the MS-II, while the solid red curve is based on the MS. The two converge well above a stellar mass of about $3 \times 10^9 M_\odot$, but at lower masses the MS underpredicts abundances because it does not resolve halos less massive than $2.3 \times 10^{10} M_\odot$, as compared to 1.9×10^8 in the MS-II. At the highest masses, the two simulations also diverge, but this is mainly due to cosmic variance and the relatively small volume of the MS-II. We estimate this uncertainty by dividing the MS into 125 sub-cubes, each of the same volume as the MS-II. The *rms* scatter among their individual stellar mass functions is given by the error bars overplotted on the green MS-II curve. Boylan-Kolchin et al. (2009) show that such differences become more prominent at high redshift. Black stars are the observed stellar mass function estimated from SDSS/DR7

Table 1. Summary of those parameters of our preferred model which were adjusted primarily to fit the observed $z = 0$ stellar mass function.

Parameter	Description	Preferred value
α	Star formation efficiency (Sec.3.4)	0.02
ϵ	Amplitude of SN reheating efficiency (Sec. 3.5)	6.5
β_1	Slope of SN reheating efficiency (Sec. 3.5)	3.5
η	Amplitude of SN ejection efficiency (Sec. 3.5)	0.32
β_2	Slope of SN ejection efficiency (Sec. 3.5)	3.5
γ	Ejecta reincorporation efficiency (Sec. 3.5)	0.3
κ	Hot gas accretion efficiency onto black holes (Sec. 3.9)	1.5×10^{-5}

by Li & White (2009), except that the masses are converted to total stellar masses as described in Appendix A of Guo et al. (2010). Note that these observed stellar masses are also based on the same Chabrier IMF used in our models, so that IMF uncertainties should not affect the comparison of the two. The error bars here include cosmic variance uncertainties and are very small, reflecting the large volume of the survey. Blue triangles are estimates based on SDSS/DR4 from Baldry et al. (2008). These include a correction for surface brightness incompleteness, which becomes significant at these low masses, but their error bars do not include cosmic variance which is quite large because of the small volume effectively surveyed for such faint galaxies. To make the comparison clearer, the lower panel of Fig. 7 shows the SDSS data (the symbols), our MS prediction (red curve) and the MS predictions of DLB07 (purple curve) all ratioed to our predictions based on the MS-II.

It is clear from Fig. 7 that adopting the MS-II stellar mass function below about $3 \times 10^9 M_\odot$ and the MS function at higher masses results in a very good match to the observational results for our preferred parameters. The fit extends over the full range of the observations from about $10^{12} M_\odot$ all the way down to about $2 \times 10^7 M_\odot$. The slope at the low-mass end is around -1.46 in the model, significantly steeper than the value of -1.155 quoted by Li & White (2009). The Baldry et al. (2008) results suggest that this may reflect the onset of incompleteness effects at the lowest masses considered by Li & White (2009). The high resolution of the MS-II allows us to predict galaxy abundances to substantially lower stellar masses. Here we show our predictions down to $10^6 M_\odot$ although there are currently no reliable observations with which to compare them. At this mass, the predicted number density is around $0.3 \text{ Mpc}^{-3} (\log M_*)^{-1}$. Galaxies even less massive than this *can* be observed in the Local Group and we show below that our model does, in fact, agree quite well with the abundance of Milky Way satellites as a function of luminosity (see Sec. 4.8).

At high stellar masses, where growth is limited by AGN feedback as in Croton et al. (2006), our model overpredicts the abundance found by Li & White (2009). This likely reflects the observational difficulty in estimating stellar masses for the most luminous *cD* galaxies in clusters. As a result of the problems with dealing with extended envelopes and crowded fields, SDSS photometry gives luminosities for such galaxies which are significantly lower (by up to one magnitude) than found in other investigations (e.g. von der Linden et al. 2007). As the lower panel of Fig.7 shows, our model agrees with these SDSS data significantly better than the older model of DLB07.

In Fig. 8 we show predictions of this same preferred model for galaxy luminosity functions in the SDSS g , r , i and z bands, comparing them with observational data from a low-redshift SDSS sample taken from Blanton et al. (2005). In all these plots we have used results from MS+MS-II at absolute magnitudes brighter than -20, where results from the two simulations converge, and results from the MS-II alone at fainter magnitudes. Given that Fig. 7 shows our model to overpredict slightly the abundance of low-mass dwarf galaxies, it is somewhat surprising that it turns out to underpredict their abundance as a function of luminosity in all four bands. Several effects may contribute to this discrepancy. One is that, as we will see later, the fraction of non-star-forming dwarf galaxies appears to be significantly larger in the model than in the SDSS data, so we are probably assigning stellar mass-to-light ratios which are too large to many dwarfs. A second is that Blanton et al. (2005) corrected their luminosity functions for incompleteness at low surface-brightness, and their corrections may be larger than those applied by Baldry et al. (2008) in the SDSS mass function estimate plotted in Fig. 7. Finally, quite small volumes are surveyed when compiling luminosity functions for dwarfs, even with the SDSS, so cosmic variance effects may be significant. The discrepancy could then in part reflect differences in large-scale structure between the small low-redshift volume surveyed by Blanton et al. (2005) and DR7. The model also noticeably overpredicts the abundance of very luminous galaxies in the g -band. These are massive galaxies undergoing merger-induced starbursts, and it is likely that our simple dust model is failing to predict enough extinction for these systems.

4.2 The stellar mass – halo mass relation

Simplified models for populating dark matter only simulations with galaxies often assume a simple relation between the stellar mass of a galaxy and the mass of the halo surrounding it – more massive halos should contain more massive galaxies at their centres. For such a model to represent galaxy clustering even approximately, it must also place galaxies at the centres of satellite subhalos, and the resolution of the simulation must therefore be good enough that a subhalo corresponding to every galaxy can be identified. Since tidal stripping often substantially reduces the masses of satellite subhalos, but plausibly has little effect on the galaxies at their centres, the stellar masses of such galaxies should be much more closely related to the maximum masses ever attained by their halos than to their current masses. This argument has led many authors to consider

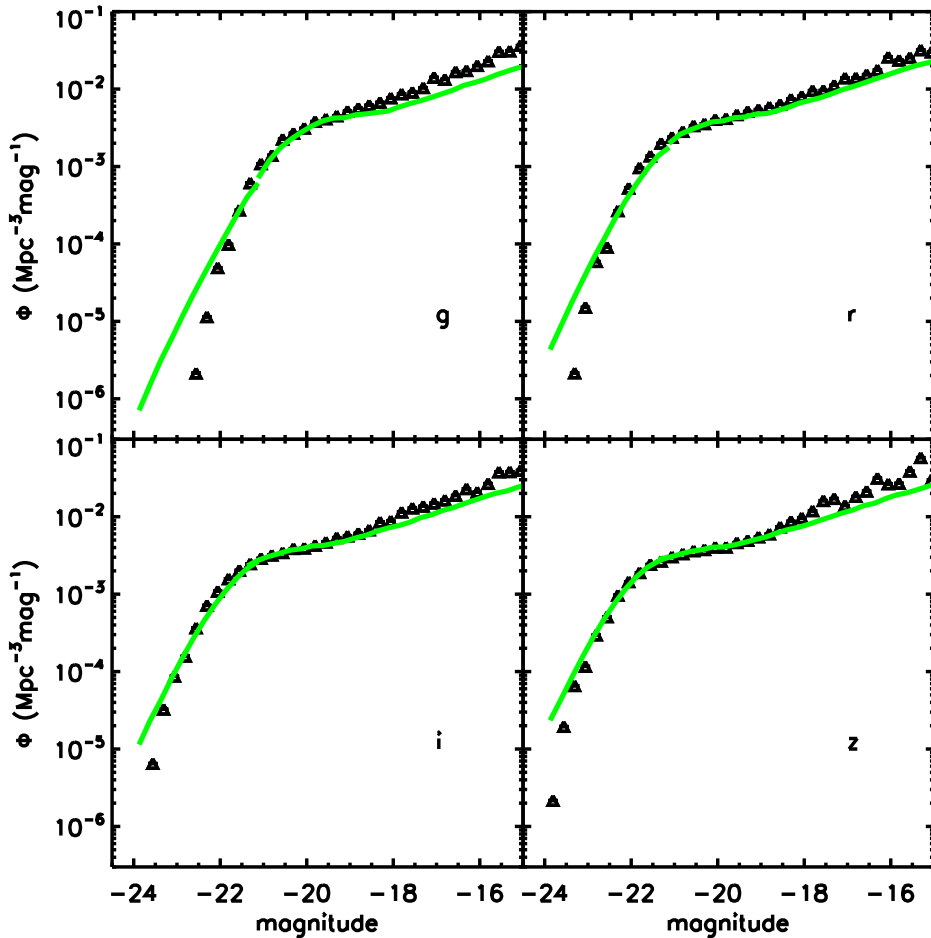


Figure 8. Galaxy luminosity functions in the SDSS *g*, *r*, *i* and *z* photometric bands. The smooth green curves are predictions from our preferred model taken from the MS+MS-II at high luminosities and from the MS-II alone at absolute magnitudes fainter than about -20 . The symbols are observational data for a low-redshift SDSS sample taken from Blanton et al. (2005).

models which populate simulations with galaxies assuming a simple monotonic relation between the stellar mass of a galaxy and this maximum past halo mass (Vale & Ostriker 2004; Kravtsov et al. 2004; Conroy et al. 2006; Wetzel et al. 2009; Moster et al. 2010; Guo et al. 2010). For cosmological simulations of high resolution, matching the (sub)halo abundance as a function of maximum past mass to the observed galaxy abundance as a function of stellar mass allows one to derive an (assumed) monotonic relation between the two masses. By using this relation to populate the simulation, one can then predict the spatial distribution of galaxies for detailed comparison with observation.

The MS-II simulation provides an unparalleled opportunity to carry through this programme because, in combination with the MS, it gives a much more precise estimate of the abundance of (sub)halos as a function of maximum past mass than has previously been available. Guo et al. (2010) matched an estimate based on both the MS and the MS-II to the SDSS stellar mass function of Li & White (2009), producing the relation between stellar mass and maximum past halo mass which we show as a blue curve in Fig. 9. For comparison, green and red symbols show the median value and the $\pm 1\sigma$ scatter of stellar mass predicted by our preferred

model at given past maximum halo mass for $z = 0$ central and satellite galaxies, respectively. Variations in assembly history and environmental influence ensure that there is significant scatter in the relation for our model; the *rms* scatter in $\log M_*$, is 0.17, 0.20, 0.24 and 0.31 for $\log M_{\text{halo}} = 14, 13, 12$ and 11 respectively. At low mass, there is a noticeable offset between the predictions for satellite and central galaxies, with satellites having systematically larger stellar masses for given maximum past halo mass. This behaviour was also present in the DLB07 model (see, Wang et al. 2006) and can be traced to the fact that low-mass satellite galaxies typically achieved their maximum halo mass at $z \sim 1$, whereas for the corresponding centrals this is typically around $z \sim 0$. Since halos are 8 times denser at $z = 1$ than at $z = 0$, their escape velocities at given mass are roughly 40% larger at the higher redshift and this reduces the efficiency with which SN feedback can expel gas, increasing the retention of baryons for star formation.

The median stellar mass predicted by our model at each maximum past halo mass is very close to the Guo et al. (2010) relation at halo masses above about $10^{11} M_{\odot}$, but lies noticeably above it at lower masses. This is because Guo et al. (2010) extrapolated the Li & White (2009) stellar mass

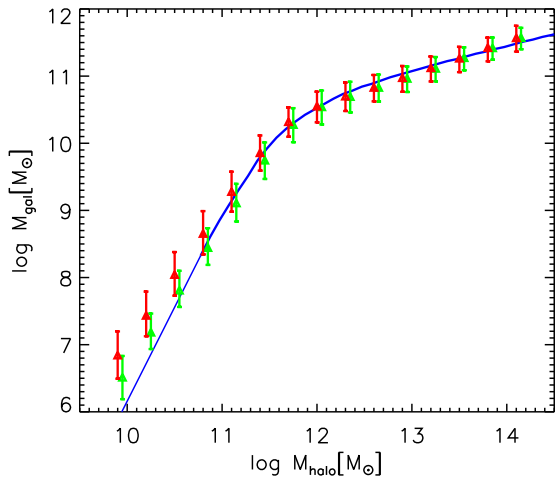


Figure 9. Galaxy stellar mass as a function of maximum past halo mass. The latter is the largest mass ever attained by the dark matter subhalo centred on the galaxy over its full history. This is almost always the mass of the subhalo at the last time its central galaxy was type 0, i.e. the present subhalo mass for current type 0 galaxies and the subhalo mass just before infall for current type 1 and 2 galaxies. Symbols with error bars show predictions from our preferred model applied to the MS-II for $\log M_* < 10$, and applied to the MS at higher masses. Green symbols are for central galaxies (type 0) while red symbols are for satellites (types 1 and 2). The blue curve is the relation derived directly from the SDSS stellar mass function and from subhalo abundances in the MS and MS-II under the assumption that the two quantities are monotonically related without scatter (Guo et al. 2010).

function to masses below $10^{8.3} M_\odot$ using their quoted slope of -1.15 , which predicts significantly fewer low-mass dwarfs than the Baldry et al. (2008) function which we plot in Fig. 7 and use to set the parameters of our preferred model. In their own comparison of a similar relation to observational data on satellite galaxy dynamics, More et al. (2009) estimated the scatter in $\log L$ for relatively massive halos ($\log M_{\text{vir}} \sim 13$) to be 0.16 ± 0.04 . This is in good agreement with the scatter actually produced by our galaxy formation model, but is considerably smaller than that predicted, for example, by the models of Bower et al. (2006) or Font et al. (2008).

4.3 Gas-phase metal abundances

In Fig. 10 we show the metallicity of the cold ISM gas as a function of stellar mass for star-forming galaxies in our preferred model. Here, we define as star-forming those galaxies with a specific star formation rate $\dot{M}_*/M_* > 10^{-11} \text{yr}^{-1}$. Observational data from Tremonti et al. (2004) and Lee et al. (2006) are represented by the solid green curve and the red diamonds, respectively. When estimating the oxygen abundance of model galaxies for comparison with these observations, we, for consistency, use the same nucleosynthetic yields and solar abundances as DLB07. Recent work has suggested that these may need to be revised (Asplund et al. 2006; Delahaye & Pisonneault 2006) but the strong-line metallicity measurements underlying the observational results in Fig. 10 have substantial and controversial uncer-

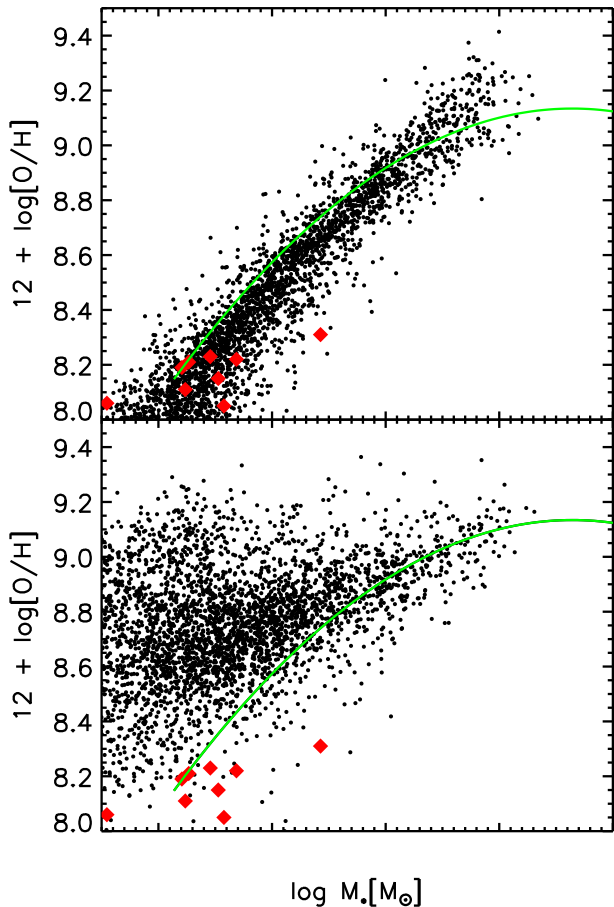


Figure 10. Cold gas metallicity as a function of stellar mass. The top panel shows results for star-forming galaxies when our preferred model is applied to the MS-II. The bottom panel shows similar results but based instead on the DLB07 model. In both panels, the solid curves represent observational results for the SDSS from Tremonti et al. (2004), while red diamonds are taken from Lee et al. (2006)

tainties, so we prefer to keep our previous assumptions so that the models can be easily compared. Results for star-forming galaxies in the MS-II are shown as small black dots in the upper panel of Fig. 10, which shows that our model appears to reproduce the tight observed relation between gas metallicity and stellar mass quite well. This is mainly due to our introducing a velocity dependence in our SN feedback prescription, which leads to less star formation and to more effective ejection of metals from low-mass galaxies, thus to lower metallicities.

For comparison, in the bottom panel of Fig. 10 we show the predictions obtained when the DLB07 model is applied to the MS-II. In this model the SN feedback efficiency is assumed to be independent of circular velocity ($\beta_1 = \beta_2 = 0$) leading to a weaker dependence of metallicity on stellar mass at low masses than our current preferred model, as well as to an overabundance of dwarf galaxies (see Fig. 1). The better apparent agreement of the DLB07 model with dwarf galaxy properties found in earlier papers turns out to have been due largely to the limited resolution of the MS.

4.4 Galaxy colours

The colours of galaxies are influenced strongly by dust, by their star-formation histories, particularly by current and recent star formation, and by the metallicities of their stars. This makes colours especially difficult to predict with models of the kind we are discussing, because they are sensitive not only to the details of stellar population synthesis, but also to assumptions about the production and quantity of dust, and about its distribution relative to the different stellar populations. While population synthesis models have solid theoretical foundations, are well developed and tested, and are probably reliable in most situations, the opposite is true for dust modelling. For this reason, rather than predicting the luminosities and colours of galaxies directly, it is often safer to make model predictions for physical properties like stellar mass and star formation rate, and to compare these with distributions inferred from observation using methods designed to be as insensitive as possible to dust.

In Fig. 11, we show a scatter plot of SDSS $u - i$ colour against stellar mass for model galaxies at $z = 0$. The upper panel includes dust extinction effects, while the middle one does not. Blue dots represent galaxies with dominant disks ($M_{\text{bulge}} < M_{\text{disk}}$), and red dots galaxies with dominant bulges ($M_{\text{bulge}} > M_{\text{disk}}$). A clear split of the population into a red sequence and a blue cloud is visible in both plots. When dust effects are included, our model predicts the reddest galaxies to be passive disk systems scattered up from the red sequence. It is notable that we predict substantial numbers of disk galaxies on the red sequence, particularly at intermediate stellar masses. This appears consistent with the fact that S0 galaxies substantially outnumber ellipticals in this stellar mass range in the local universe (e.g. Dressler 1980), although real S0's rarely have as much dust and gas as our model is assigning them. As in DLB07, the most massive galaxies are bulge-dominated and lie on the red sequence. There are also a few massive bulge-dominated galaxies with bluer colours, corresponding to ellipticals that have undergone a recent star-formation event, the equivalent of the E+A galaxies seen locally (e.g. Zabludoff et al. 1996). Finally at low stellar masses we predict both sequences to be well populated. As we will see, the fraction of passive dwarf galaxies in our model appears larger than observed. To compare with observation, we show results from SDSS/DR4 in the bottom panel. These have been down-sampled to correspond to a volume-limited subset with stellar masses above $10^{9.5} M_{\odot}$ as in Weinmann et al. (2009). The numbers are quite small because the reddest galaxies at this lower mass limit fall within the spectroscopic sample only at very low redshift. Clear differences with the models appear in the slope of the red sequence and in the number of fainter red-sequence galaxies.

To explore this discrepancy with observation in more detail, Fig. 12 shows the distributions of $u - i$ (including dust extinction) for galaxies in 8 stellar mass ranges spanning four orders of magnitude in stellar mass. The solid histograms are constructed from our preferred model applied to the MS (for $\log M_* > 10.0$) and to the MS-II (at lower masses) while the dashed histograms are compiled from SDSS/DR7 including $1/V_{\text{max}}$ corrections so that they correspond to volume-limited statistics. All histograms are normalised to have unit integral. For galaxies in the stel-

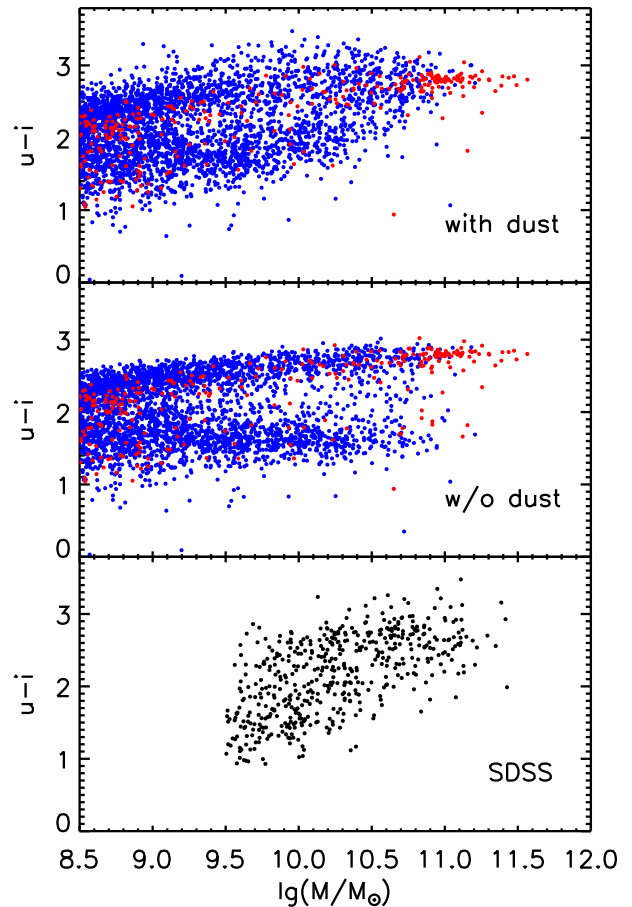


Figure 11. $u - i$ colour as a function of stellar mass for galaxies in our preferred model applied to the MS-II. The upper and central panels are for model colours including and excluding dust extinction effects, respectively. In each panel, red and blue dots refer to bulge-dominated and disk-dominated galaxies, respectively, with the split set at equal stellar masses for the two components. The bottom panel is for a volume-limited subset of SDSS/DR4 with no distinction by morphology.

lar mass range $9.5 < \log M_* < 11.0$ which contains the bulk of all stars, our predictions for the $u - i$ distribution are in reasonable agreement with observation, despite our over-simplified dust model. At lower masses, the fraction of red galaxies is clearly larger in our model than observed. A substantial fraction of dwarfs (roughly half) are predicted to finish their star formation early and to become passive. The observed fraction of such passive dwarfs is substantially smaller. At the highest masses, the SDSS galaxies are redder than our model predicts. In the model most of these galaxies have mean stellar ages greater than 10 Gyr and stellar metallicities of order $0.5 Z_{\odot}$. The real galaxies are more metal-rich, but for the population synthesis model we are using, a 12 Gyr old population with twice solar metallicity has $u - i = 3.07$, thus metallicity and age effects are insufficient to explain the discrepancy and no significant dust effects are expected. Photometric or K-correction problems may be affecting these galaxies which are typically at $z \sim 0.2$. Note that at lower mass, the red tails of the distributions correspond to the (unrealistically) reddened passive disk galaxies

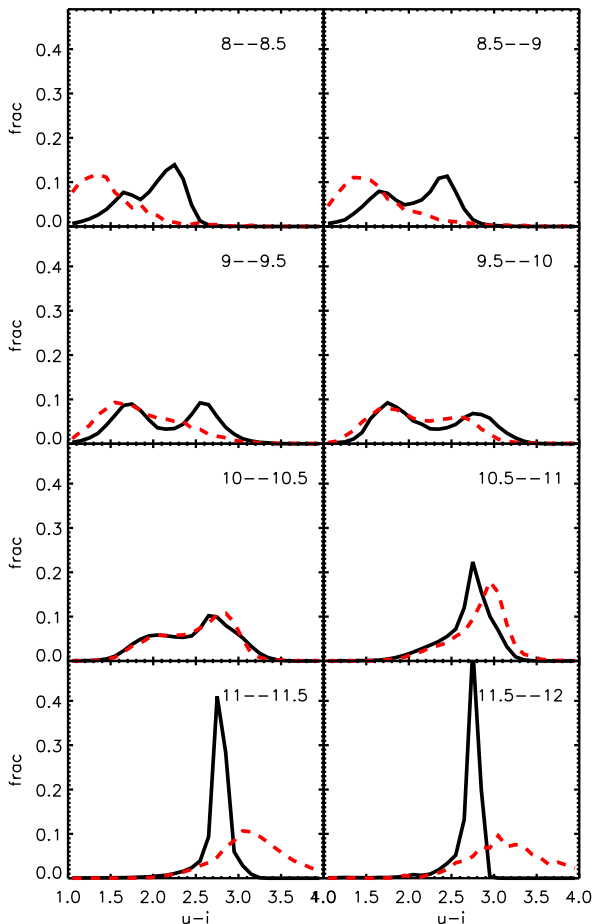


Figure 12. $u - i$ colour distributions as a function of stellar mass. Solid black curves show the distributions predicted by our preferred model (including extinction effects) applied to the MS (above $\log M_* = 10.0$) and the MS-II (at lower masses), while dashed red curves are distributions compiled from SDSS/DR7. The range in $\log M_*/M_\odot$ corresponding to each panel is indicated at top right.

seen in the upper panel of Fig. 11. This tail is absent at the highest masses where the galaxies no longer have gas disks.

4.5 Tully-Fisher Relation

There has been a long-standing debate about the ability of galaxy formation models in a CDM context to reproduce simultaneously the observed abundance and Tully-Fisher (TF) relation of disk galaxies (Kauffmann et al. 1993; Cole et al. 1994; Navarro & Steinmetz 2000; Cole et al. 2000; Blanton et al. 2008). We have shown above that our preferred model reproduces the observed galaxy luminosity functions in four SDSS bands at $z = 0$. In this section, we study whether it simultaneously produces a relation between r -band luminosity and maximum circular velocity which is consistent with that observed for isolated spiral and irregular systems. Early semi-analytic work on the TF relation (e.g. Kauffmann et al. 1993; Cole et al. 1994; Somerville & Primack 1999) took the disk rotation velocity to be V_{vir} , the

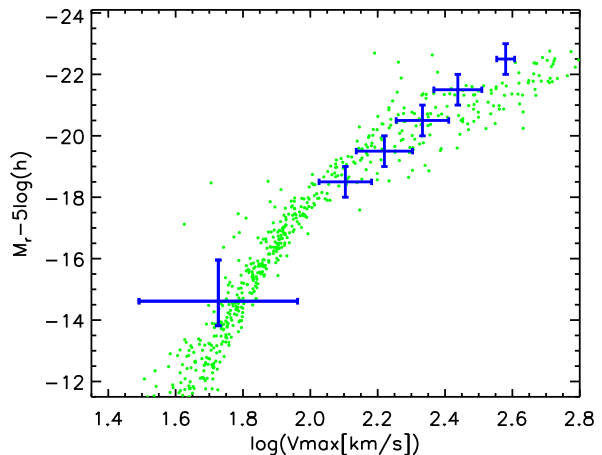


Figure 13. r -band Tully-Fisher relation. Blue symbols with error bars are observational results for isolated disk galaxies taken from Blanton et al. (2008) and from Springob et al. (2007). The vertical bar on each symbol shows the bin in absolute magnitude considered, while the horizontal bar is centred on the median and shows the *rms* scatter of $\log V_{\text{max}}$ for the galaxies within that bin. Green dots are results for central (type 0) late-type galaxies from our preferred model applied to the MS (brighter than -21) and to the MS-II (for fainter galaxies). For the model galaxies V_{max} is the maximum circular velocity of the hosting dark halo.

circular velocity of its halo at the virial radius. In the DLB07 model a reasonable match to the observed relation was instead found by identifying the disk rotation velocity with the *maximum* circular velocity of its halo (see Croton et al. 2006, and its erratum). On the other hand, Cole et al. (2000) found that if baryon condensation is assumed to cause halo contraction according to the standard simple formula (Barnes 1984; Blumenthal et al. 1986) the models are no longer able to reproduce the Tully-Fisher relation and the luminosity function simultaneously. As discussed in Sec. 3.3, the simplified model of adiabatic contraction adopted by Cole et al. (2000) appears to overestimate the effect of baryons, and at least some recent simulations suggest that the maximum halo circular velocity found in an equivalent dark matter only simulation may be a good approximation to the disk rotation velocity (e.g. Tissera et al. 2010). Here we use this maximum circular velocity as our disk rotation velocity surrogate for the TF relation.

We concentrate on central galaxies in the model and compare to observations of isolated systems, because, as noted by Blanton et al. (2008) and others Einasto et al. (1974), dwarf satellite galaxies appear systematically gas-poor and to have systematically lower rotation velocities relative to isolated dwarfs of similar stellar mass. This is presumably related to the various stripping mechanisms discussed above. In order to keep the test simple, it seems wise to concentrate on galaxies where such effects are absent.

We select central galaxies in our model for which the r -band absolute magnitude of the bulge is at least 1.5 magnitudes fainter than that of the galaxy as a whole, and, as before, we assume the rotation velocity of the disk to be V_{max} , the maximum circular velocity of its host halo. In massive spirals, where baryons dominate in the visible regions, this

may underestimate the rotation velocity because we do not take the mass of the baryons into account. In dwarf galaxies it may, in contrast, overestimate the rotation velocity because baryonic effects are weaker and the observable HI may not extend out to the maximum of the halo circular velocity curve. For simplicity, we neglect such effects here. The Tully-Fisher relation predicted in our preferred model by these assumptions is shown using green dots in Fig. 13. At absolute magnitudes above -21 the data are taken from the MS, while for fainter galaxies they are taken from the MS-II. Observational data for relatively bright galaxies from Springob et al. (2007) and for isolated dwarfs from Blanton et al. (2008) are shown by blue symbols. The vertical bar on each symbol represents the absolute magnitude bin considered and is positioned at the median $\log V_{\max}$ of the observed galaxies in that bin. The horizontal bar shows the $\pm 1\sigma$ scatter in $\log V_{\max}$ within the bin.

It is striking that our model, although clearly not a power law, nevertheless agrees reasonably well with the data over an absolute magnitude range of about eight magnitudes. There is no evidence for any major problem, even for dwarf galaxies with $M_r \sim -15$. This is somewhat unexpected, and is due in part to the fact that Blanton et al. (2008) excluded dwarf satellite (as opposed to central) galaxies for which the measured rotation velocities *are* significantly lower at the faintest magnitudes. A more careful comparison does show some discrepancies, however. At high circular velocities ($V_{\max} \sim 250\text{km/s}$ or more) model galaxies have a larger scatter in luminosity than the observations. The brightest real galaxies have smaller rotation velocities than we predict, perhaps because we are stopping star formation too efficiently in at least some massive systems. At the lowest luminosities the simulation predicts slightly higher rotation velocities and considerably less scatter than is observed. This may reflect the fact that HI data often do not reach the peak of the rotation curve in these systems, although the current sample of isolated dwarfs is probably too sparse to draw reliable conclusions.

4.6 Profiles and mass functions in rich clusters

An important aspect of our galaxy formation models is associated with the disruption and merging of substructures. When tidal effects destroy a dark matter subhalo, we continue to follow the properties of its central galaxy, tracking its position and velocity using those of the particle which was most bound to the subhalo when it was last seen. Such “orphan” galaxies may merge with another galaxy (usually the central galaxy of the main system) or may themselves be tidally destroyed, when specific conditions are satisfied (see sections 3.6.2 and 3.7). These procedures account for the fact that dark matter subhalos are often prematurely disrupted in our simulations both for numerical reasons (resolution may be insufficient to follow tidal stripping down to the scale of the central galaxy) and for astrophysical reasons (dissipation associated with galaxy formation may make the stellar components more resistant to disruption). Thus at any given time our galaxy catalogues contain a population of orphan (or type 2) galaxies which are concentrated in the inner regions of massive halos.

The large size of our two simulations and the factor of 125 difference in their mass resolution makes it possible

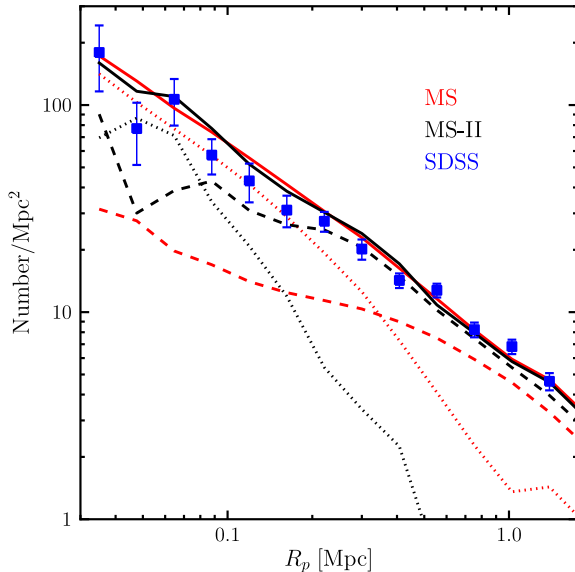


Figure 14. Projected galaxy number density profiles for samples of massive clusters from the MS (red lines) the MS-II (black lines) and from the SDSS (blue symbols with error bars). Observational and model clusters are selected in the same way and are not scaled before stacking (see text for details). Solid lines are for all model galaxies with $M_* > 1.2 \times 10^{10} M_\odot$, while dashed and dotted lines split them into galaxies with surviving dark matter subhalos and orphans, respectively. Note the excellent agreement in mean profile between the MS and MS-II despite the very different number of orphans in the two simulations. The SDSS profiles here have been corrected for the spectroscopic incompleteness of the survey, which varies as a function of projected radius and reaches 60% near cluster centre. The error bars reflect the uncertainty in the mean estimated from the scatter among the 31 SDSS cluster profiles.

to carry out convincing tests of these procedures for the first time. Appendix A presents the fraction of galaxies of different types in our preferred model. For stellar masses in the range $9.5 < \log M_*/M_\odot < 11$ where both simulations have good statistics, they show similar fractions of all galaxies to be satellites, but the fraction of these satellites which are orphans changes from 52% in the MS to 25% in the MS-II (at $\log M_*/M_\odot = 9.5$) or from 27% to 17% (at $\log M_*/M_\odot = 11$). Here we test for numerical convergence in a considerably more extreme situation by comparing the number density profiles predicted for rich clusters in the MS and the MS-II. Another sensitive test, based on counts of close pairs, is presented below in section 4.9.

In order to facilitate comparison with real clusters from the SDSS, we have implemented a simple “observational” cluster finder on our simulations, designed to find objects with virial masses in the range $14 < \log M_{\text{vir}}/M_\odot < 14.5$. We take all galaxies with stellar masses above $1.2 \times 10^{10} M_\odot$ and we view their distribution in “redshift space” where the x and y coordinate directions are considered transverse to the “line-of-sight” and the z peculiar velocity is added to the Hubble constant times the z -coordinate to produce a pseudo-recession velocity. We then consider all galaxies as

potential cluster centres, and we count neighbours within a surrounding cylinder of radius $r_p = 1.5$ Mpc and line-of-sight velocity difference ± 1200 km/s, weighting by an “optimal” filter $F(r_p)$ which we take to be an NFW approximation to the projected mass distribution of the target clusters. Potential centres are ranked by this weighted neighbour count and those lying within the cylinder of a higher ranked neighbour are eliminated. The MS is then used to relate the corresponding unweighted counts N_c to halo mass in order to identify the count range $45 \leq N_c \leq 105$ corresponding to $14 < \log M_{\text{vir}}/M_\odot < 14.5$. This algorithm can be used almost unmodified on a stellar-mass-limited sample of 39 600 SDSS galaxies from DR7 with $0.01 < z < 0.06$ and $M_* > 1.2 \times 10^{10} M_\odot$. The only complication is that the SDSS spectroscopy becomes significantly incomplete in the inner regions of clusters so that a completeness correction must be applied. This can be estimated from the overall spectroscopic completeness as a function of r_p within the stacked regions. These procedures select 2251, 61 and 31 clusters in the MS, the MS-II and the SDSS, respectively³. The effective SDSS volume searched is 6×10^6 Mpc³; given the expected cosmic variance expected for the cluster count in a volume of this size ($\sim 25\%$ rms), and the rather large amplitude $\sigma_8 = 0.9$ adopted in the simulations, the observed and simulated cluster abundances appear quite consistent.

In Fig. 14 we show mean projected number density profiles for stacks of the clusters in these different sets. Solid lines show the mean profiles for the two simulations, while dashed and dotted profiles split these profiles into galaxies with and without associated dark matter subhalos. Red curves refer to the MS and black curves to the MS-II. The agreement in the total profiles is remarkable – certainly better than one might have expected since the dashed and dotted profiles show that orphans make a much larger contribution to the MS profiles (where they dominate for $r_p < 350$ kpc) than to the MS-II profiles (where they dominate only for $r_p < 80$ kpc). Within a projected radius of 1.5 Mpc, 37% of all cluster galaxies more massive than $10^{10} M_\odot$ are orphans in the MS but only 14% in the MS-II. The fact that the total profiles agree so well thus demonstrates that the survival times and positions that we assign to our orphans are appropriate.

The SDSS clusters in Fig. 14 are shown by the blue symbols with error bars indicating the uncertainty in the mean profile due to cluster to cluster variations. The agreement with the simulations is quite good, although there may be an indication that the SDSS clusters are somewhat less concentrated than our models. This may be an indication that the σ_8 value adopted in the simulations is somewhat too high (see also Section 4.9 below).

The biggest halo in the MS-II has a mass of $\sim 10^{14.8} M_\odot$, similar to that of the Coma cluster, and contains over 119 million particles. Its substructures are thus very well resolved. Here we use this biggest halo to investigate whether the galaxy stellar mass function inside clusters is expected to differ significantly from that of the galaxy population as a whole. It is well known that the most massive galaxies

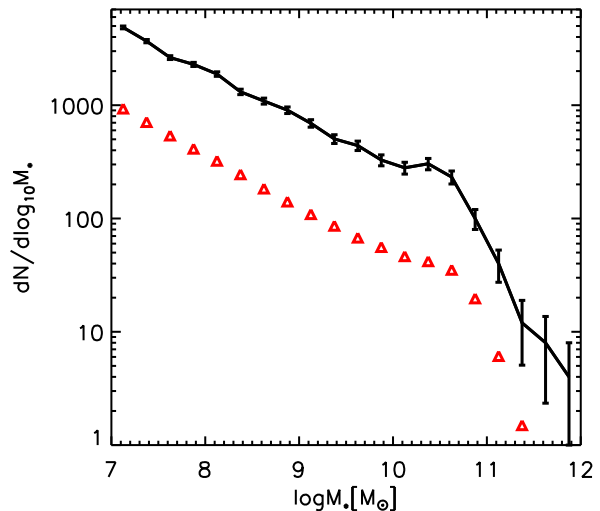


Figure 15. The stellar mass function of galaxies in a rich cluster. The solid curve links counts in 0.25dex bins for galaxies within $R_{\text{vir}} = 2$ Mpc of the centre of the most massive cluster in the MS-II according to our preferred galaxy formation model. Error bars indicate Poisson uncertainties in these counts. Red open triangles represent the general stellar mass function of galaxies constructed from the MS-II as a whole. This has been renormalized arbitrarily to allow its shape to be compared to that of the cluster stellar mass function.

occur exclusively in rich clusters, and that cluster populations have systematically different star formation histories and morphologies to field galaxies. Nearby clusters also appear to contain a population of small dwarf ellipticals which are not found in less dense environments (e.g. Binggeli et al. 1990). Thus it is interesting to see whether our galaxy formation model predicts differences which might correspond to these observations, and, in particular, to see if the relative number of dwarf galaxies in a rich cluster is predicted to differ from that in the “field”.

We study this in Fig. 15. The solid curve is the stellar mass function for galaxies within $R_{\text{vir}} = 2$ Mpc of the centre of this massive cluster, with error bars indicating the Poisson uncertainty in the count in each bin. The slope at the low mass end is around -1.4, which is higher than the observed *r*- or *R*-band slope for galaxies in the Coma cluster: ~ 1.16 (Beijersbergen et al. 2002; Mobasher et al. 2003), but perhaps consistent with recent observational estimates based on the SDSS data for nearby X-ray-selected clusters (Popesso et al. 2006). At very faint magnitudes the slope in the Coma cluster may be steeper (Adami et al. 2007; Jenkins et al. 2007; Milne et al. 2007). Given the large dispersion in observational results, our model seems quite compatible with the data. The triangles show the overall stellar mass function of the MS-II, renormalized for ease of comparison with the cluster result. The shapes of the two stellar mass functions are very similar, both the faint-end slope and the break at high mass. This echoes the results found for the infrared luminosity function of the Coma cluster by Bai et al. (2006). This is interesting, since both observations and the simulations of this paper show substantial differences in colour and morphology between clusters and the field. In the simu-

³ In order to improve the statistics, we include three orthogonal projections of the MS-II data, so the mean number of clusters per MS-II volume is 20.3.

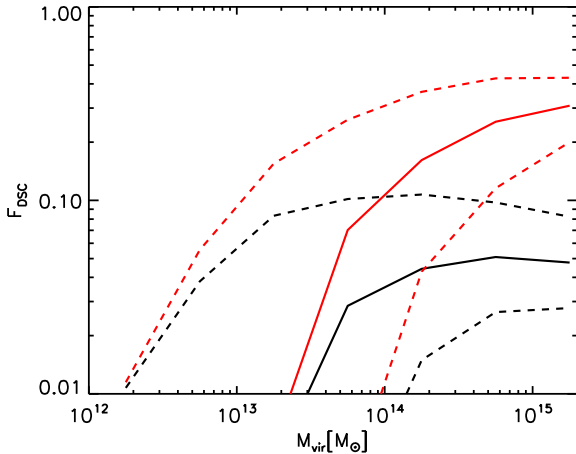


Figure 16. The stellar mass fraction in intergalactic stars as a function of virial mass for clusters. The solid black line shows the fraction of all stars within R_{vir} which are assigned to the intracluster component when our preferred model is applied to the MS. Dashed black lines show the 16 and 84% points of the distribution of this fraction. Solid and dashed red lines show the same statistics but for the fraction of stars in the main subhalo of each cluster which are associated with its diffuse component, rather than with its central galaxy.

lations over 95% of cluster galaxies within R_{vir} are passive. This fraction seems overly large in comparison to observation (e.g. Hansen et al. 2009), again reflecting the fact that the passive galaxy fraction in general is somewhat too high in our model.

4.7 Intracluster Light

Recent observations of diffuse intracluster light and of intracluster stars (Zibetti et al. 2005; Gerhard et al. 2005; Mihos et al. 2005; Gonzalez et al. 2005; Aguerri et al. 2006; Gonzalez et al. 2007; McGee & Balogh 2010) indicate that a significant fraction of all cluster stars lie between the galaxies, but they disagree about the exact amount. It seems likely that such stars must be the remains of disrupted galaxies, and our model now includes a treatment of the tidal disruption process. In Fig. 16, we show the fraction of cluster stars in the intergalactic component as a function of cluster virial mass. We consider two different fractions here. The black lines refer to the fraction by mass of all stars within R_{vir} which are assigned to the intergalactic component. The solid curve is the median value at each M_{vir} , while the dashed lines indicate the 16 and 84% points of the distribution. This intracluster fraction increases with cluster mass and has a large scatter in low-mass clusters. In our preferred model (here applied to the MS) around 5-10% of all stars in clusters with $M_{\text{vir}} > 5 \times 10^{14} M_{\odot}$ are in the intracluster component and the dependence on cluster mass is quite weak. In less massive systems this fraction drops very rapidly, reaching 1% in groups of mass $3 \times 10^{13} M_{\odot}$. Both the trends and the value are within the scatter of the observational results cited above.

Fig. 16 also shows another fraction of interest. The red

curves show the median and the 20 and 80% points of the distribution of the fraction of all the stars in the main subhalo which are associated with the diffuse component, rather than with the central galaxy. This can be considered as a proxy for the fraction of the stellar mass of the cD galaxy which is associated with its extended envelope. This fraction also increases with cluster mass, ranging from $\sim 10\%$ in clusters with $M_{\text{vir}} \sim 10^{14} M_{\odot}$ to 30% in clusters with $M_{\text{vir}} \sim 1.4 \times 10^{15} M_{\odot}$. Thus, in the richest clusters, the mass in intergalactic stars is comparable to the stellar mass of the main body of the central galaxy, or, alternatively, the extended envelope of the cD galaxy contains about half of its stars. In galaxy groups, this fraction decreases rapidly with decreasing virial mass, reaching 1% in groups of mass $2 \times 10^{13} M_{\odot}$.

4.8 Luminosity function of Milky Way satellites

The abundance of the very lowest mass galaxies can be measured observationally only in the Local Group, in particular, in the halo of the Milky Way. The apparent discrepancy between the relatively small number of observed satellites and the many dark matter subhalos predicted in a Λ CDM cosmogony has been promoted as “the missing satellite problem”, a possible flaw in the concordance structure formation model (Moore et al. 1999; Klypin et al. 1999), despite earlier suggestions that it might rather reflect the astrophysics of galaxy formation in weak potential wells (Kauffmann et al. 1993). Over the last decade new observational results, primarily from the SDSS, have increased the directly observed number of satellites by almost a factor of two and the estimated total number of satellites by about a factor of four (e.g. Koposov et al. 2008). At the same time, improved simulations have increased the predicted number of subhalos by a factor of 1000 (e.g. Springel et al. 2008). Thus the discrepancy has grown. Our galaxy formation models make it possible to address this issue in the context of the more general problem of matching the low-mass end of the stellar mass function of galaxies. This is because the MS-II contains several thousand isolated galaxies similar in mass to the Milky Way, and its resolution turns out to be (just) sufficient to get predictions for objects with stellar masses comparable to those of the observed Milky Way satellites.

In the MS-II, there are around 7000 halos with virial mass within a factor of three of that estimated for the halo of the Milky Way (see Boylan-Kolchin et al. (2010) for an analysis of the properties of these halos and their substructure). In order to make a detailed comparison, we select all disk-dominated ($M_{*,\text{disk}} > M_{*,\text{bulge}}$) central galaxies with total stellar mass between 4 and $8 \times 10^{10} M_{\odot}$. (The stellar mass of the Milky Way is estimated to be $5 \times 10^{10} M_{\odot}$ (Flynn et al. 2006).) This provides us with a sample of 1603 “Milky Ways” which have median halo mass $M_{\text{vir}} = 1.30 \times 10^{12} M_{\odot}$ with lower and upper quartiles at 0.90 and $2.18 \times 10^{12} M_{\odot}$. For the purposes of this section, all galaxies within 280 kpc of each “Milky Way” are defined to be its satellites. Fig. 17 shows the cumulative V -band luminosity function of these satellite systems in our preferred model and in two variations with different assumptions about reionization. Specifically, we plot the median and the 10 and 90% points of the distribution of satellite counts as a function of limiting absolute magnitude, M_V . A dashed red curve plotted for

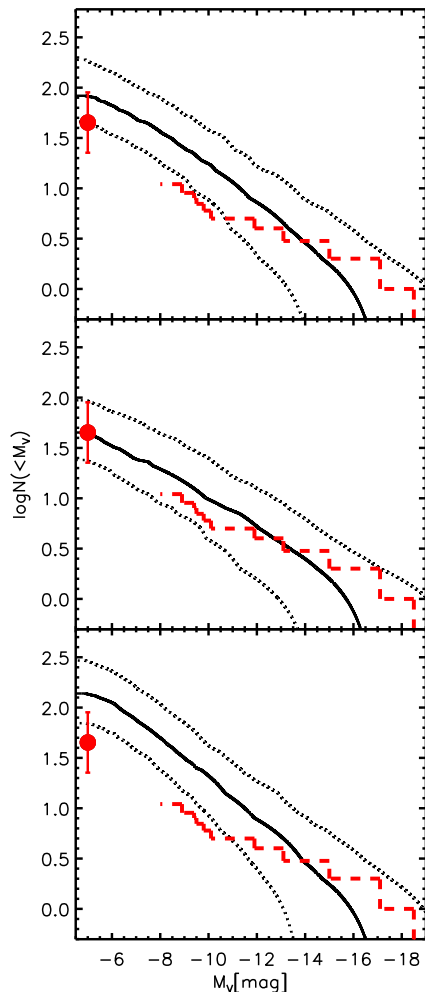


Figure 17. Cumulative luminosity functions for the Milky Way satellite system, defined to consist of all galaxies within 280 kpc of the Galactic Centre. Simulated “Milky Ways” are taken to be disk-dominated central galaxies with stellar masses between 4 and $8 \times 10^{10} M_{\odot}$. Solid curves give the median satellite count predicted above each absolute magnitude, while dotted curves delineate the 10% and 90% tails of the count distribution. The upper panel gives results for our preferred model applied to the MS-II. This assumes the effects of reionization to be as advocated by Okamoto et al. (2008). In the central panel we show what happens if we instead use the reionization prescription of Gnedin (2000), keeping all other model parameters fixed. Reionization effects are weaker in the Okamoto et al. (2008) model than in that of Gnedin (2000). More detailed discussion of these two recipes can be found in Sec. 3.1. For the lower panel, reionization is assumed to have no effect on galaxy formation. In each panel the cumulative luminosity function for the 11 “classical” satellites of the Milky Way is shown as a stepped red curve ending at $M_V \sim -8$. The abundance of satellites with $M_V < -5$ estimated by Koposov et al. (2008) is indicated by a large filled red circle. Because of the substantial and uncertain completeness correction needed to make this estimate, we have arbitrarily assigned it an error bar of a factor of two.

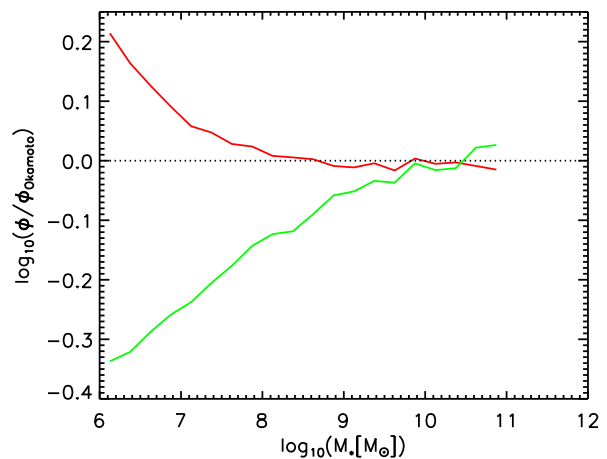


Figure 18. The effects of reionization on the low-mass end of the stellar mass function of galaxies. The red curve is the ratio of the stellar mass function predicted for the MS-II by a model excluding the effects of reionization to that predicted by our preferred model which is identical except that reionization is included following the prescription of Okamoto et al. (2008). Reionization changes the abundance of galaxies only at stellar masses below $10^8 M_{\odot}$. Effects are stronger if the prescriptions of Gnedin (2000) are used instead, as in DLB07. This is shown by the green curve which gives the ratio of the abundances predicted for this model to those predicted by our preferred model. Above $10^8 M_{\odot}$ the effects remain below 20%.

$M_V < -8$ represents the cumulative luminosity function of the 11 “classical” Milky Way satellites. To this limit, the observed sample is thought to be (almost) complete. We also use a large filled red circle to indicate the estimate of 45 Milky Way satellites with $M_V < -5$ and $r < 280$ kpc from Koposov et al. (2008). This estimate required a large and uncertain incompleteness correction, so we have arbitrarily assigned it an error bar of a factor of two.

The top panel of Fig. 17 shows results for our preferred model which assumes the Okamoto et al. (2008) prescriptions when estimating the effects of reionization. The predicted satellite abundance is consistent with observation all the way from bright LMC/M33-like systems down to $M_V \sim -11$, even though model parameters were set to match the general galaxy stellar mass function rather than Local Group data. For fainter systems, the observational estimates are close to the lower 10% point of the predicted counts, but, as just noted, the Koposov estimate has a substantial intrinsic uncertainty. In addition the classical satellite count may well have missed a one or two systems behind the Galactic Plane. As the middle panel shows, if we substitute the Gnedin (2000) parameters used by DLB07 for those of Okamoto et al. (2008), the predicted number of faint galaxies is reduced, and the match to the observational estimates is almost perfect. However, Okamoto et al. (2008) and Hoft et al. (2006) argue that the simulations of Gnedin (2000) substantially overestimated the extent to which an ionizing background suppresses the accretion of gas onto small haloes. If, on the other hand, we neglect the effects of reionization altogether, the bottom panel shows the disagreement with the observational data to worsen only at

the faintest magnitudes. The median count of satellites with $M_V < -5$ is predicted to be about four times the Kopevich estimate, but brighter than $M_V \sim -10$, the abundances are almost unchanged from our preferred model. Thus, if Okamoto et al. (2008) are right, reionization has a significant effect only on the very faintest galaxies. This is consistent with results of previous work (Bullock et al. 2000; Somerville 2002; Benson et al. 2003; Gnedin & Kravtsov 2006; Okamoto et al. 2010)

We explore this point further in Fig. 18, which shows how reionization modelling affects the low-mass end of the overall stellar mass function. We plot the factor by which the galaxy abundance in the MS-II is changed as a function of stellar mass if our preferred model, which uses the Okamoto et al. (2008) reionization parameters, is altered to use those of Gnedin (2000), as in DLB07 (green line), or to neglect the effects of reionization altogether (red line). In our preferred model, reionization affects the abundance of galaxies noticeably only below about $10^7 M_\odot$. The stronger effects implied by the Gnedin (2000) recipe, reduce the abundance by about 20% already at $10^8 M_\odot$, but remain small for more massive systems. Thus we conclude that reionization has very little effect on galaxies similar to the brighter Local Group dwarfs, but may significantly affect the abundance of the fainter dwarf spheroidals.

4.9 Correlation Functions

The SDSS has revolutionised our knowledge of the nearby galaxy population not only by providing quantitatively reliable data for galaxy abundances as a function of luminosity, stellar mass and colour over the full range from dwarfs to cD galaxies, but also by providing precise measurements of the spatial clustering of galaxies as a function of their luminosity and colour on scales from 20 kpc to 30 Mpc and beyond. With simulations the size of the MS and the MS-II, our galaxy formation models make equally precise predictions for the clustering of simulated galaxies as a function of their physical properties. Comparing observation and simulation provides powerful constraints on the galaxy formation modelling. No modern semi-analytic or hydrodynamic simulation of the formation of the galaxy population should be considered viable unless it demonstrates at least adequate agreement, not only with stellar mass, luminosity and color distributions, but also with clustering as a function of galaxy properties.

In Fig. 19 we compare the projected autocorrelation of stellar mass in the final release of the SDSS to the results we obtain for our preferred galaxy formation model. In the upper panel, red and blue symbols are results from the MS and MS-II, respectively; the black solid line shows the SDSS/DR7 measurement from Li & White (2009). The error bars on the latter include the effects of counting noise and cosmic variance and are impressively small. This is remarkable because small-scale correlations are dominated by the distribution of satellite galaxies near halo centre, where one might have expected resolution effects to cause substantial differences. For example, the number of type 2 (orphan) galaxies differs substantially between the two simulations (see Appendix A). In part, the agreement reflects the fact that, as Li & White (2009) show, the main contribution to the autocorrelation of stellar mass comes from galaxies with

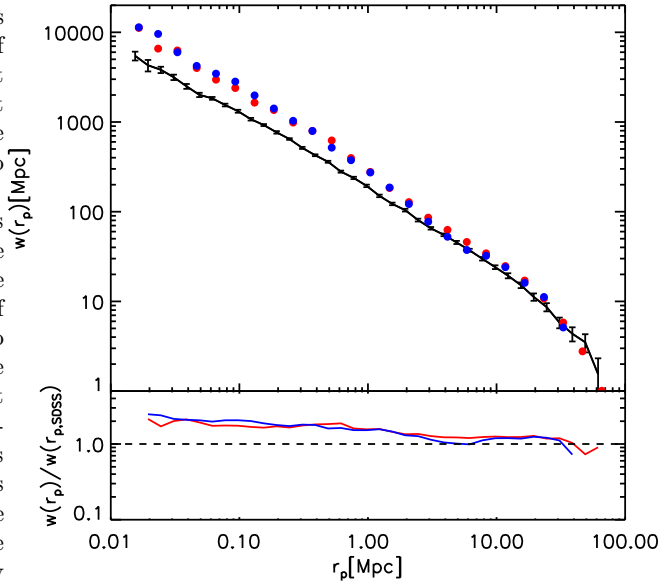


Figure 19. The projected autocorrelation function of stellar mass (upper panel). Blue and red circles show results from our preferred model applied to the MS-II and to the MS respectively. Numerical convergence is excellent, even on scales below 100 kpc. An estimate from the final release of the SDSS is shown by a black solid line joining points with error bars which include both counting noise and cosmic variance (Li & White 2009). On large scales our model overestimates the observed amplitude of clustering by 10 to 20%. On small scales the discrepancy rises to a factor of two. In the lower panel we show the ratio of the two model autocorrelation functions to the SDSS estimate.

individual stellar masses similar to the Milky Way, and thus well above the resolution limit of the MS (see the stellar mass functions in Sec. 4.1 and the mass-dependent correlation functions presented below). For $r_p > 2$ Mpc, where the correlations are produced by galaxies inhabiting different halos (thus typically both type 0 galaxies), the model autocorrelation function is 10 to 20% higher than that observed. The small difference between the MS and the MS-II on these scales may reflect the effect of cosmic variance due to the relative small box size of the MS-II. On smaller scales where the correlations are dominated by galaxy pairs inhabiting the same halo (thus typically type 0 – type 1, or type 0 – type 2 pairs) the discrepancy grows, reaching a factor of 2 at $r_p < 100$ kpc. This suggests an overdominance of 1-halo relative to 2-halo pairs in comparison to the observations, arguing, perhaps, for a lower value of σ_8 than used in the MS cosmology (see Li & White 2009).

We investigate the source of this discrepancy further in Fig. 20, which shows projected autocorrelation functions for galaxies in a set of disjoint stellar mass ranges, as indicated by the labels in each panel. Black solid and blue dashed curves give the predictions obtained by applying our preferred galaxy formation model to the MS and to the MS-II, respectively. Corresponding $1/V_{\max}$ -weighted estimates from the full SDSS/DR7, obtained using the techniques of Li et al. (2006), are shown by symbols with error bars. Here the errors are estimated from a set of 80 mock SDSS surveys and

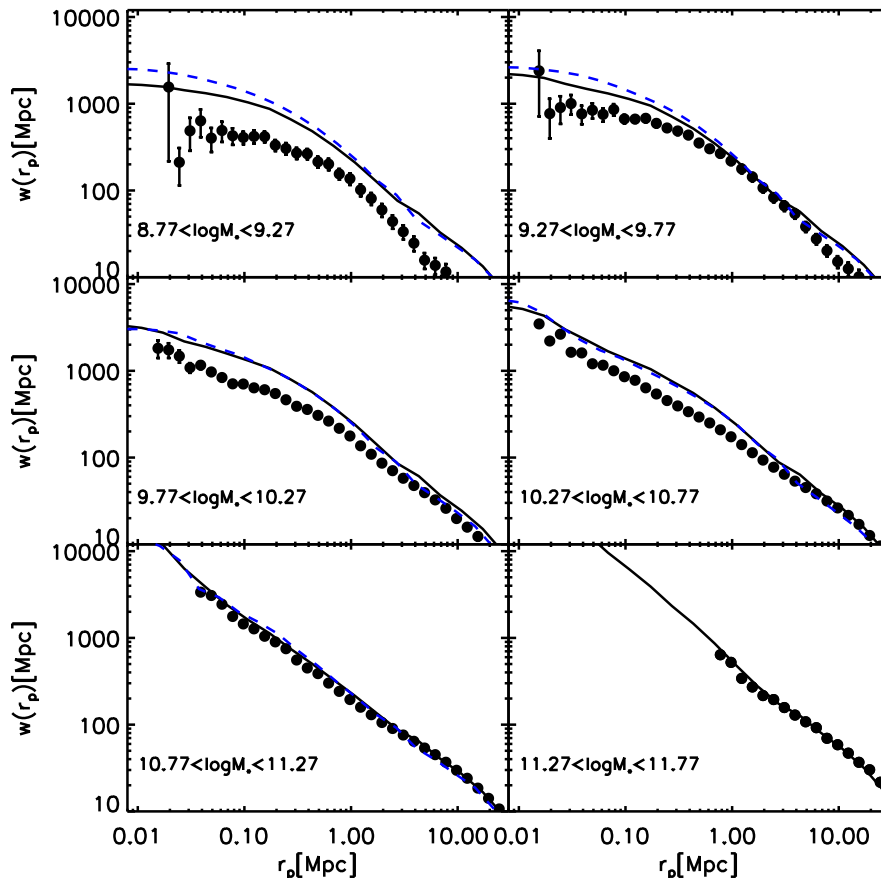


Figure 20. Projected autocorrelation functions for galaxies in different stellar mass ranges. Black solid and blue dashed curves give results for our preferred model applied to the MS and the MS-II, respectively. Symbols with error bars are results for SDSS/DR7 calculated using the same techniques as in Li et al. (2006). The two simulations give convergent results for $M_* > 6 \times 10^9 M_\odot$. At lower mass the MS underestimates the correlations on small scales but still matches the MS-II for $r_p > 1$ Mpc. The model agrees quite well with the SDSS at all separations for $M_* > 6 \times 10^{10} M_\odot$, overestimating the correlations slightly on small scales, but at smaller masses the correlations are overestimated substantially, particularly at small separations.

so should, in principle, include cosmic variance effects. This becomes a significant issue at the smallest masses. No result is shown for the MS-II in the most massive bin, because it contains too few galaxies to give a meaningful estimate. Results from the two simulations converge for galaxies more massive than $6 \times 10^9 M_\odot$. For smaller masses the MS underpredicts the correlations on small scales but still agrees with the MS-II for $r_p > 1$ Mpc. This indicates that resolution limitations begin to affect satellite galaxies in the MS at higher stellar mass than central galaxies.

For $M_* \geq 6 \times 10^{10} M_\odot$ the model autocorrelations agree with the SDSS at all separations to better than about 20%. For $M_* > 6 \times 10^9 M_\odot$, simulation and observation continue to agree at about the 20% level for $r_p > 2$ Mpc. This shows that the relation between halo mass and central galaxy mass shown in Fig. 9 leads to autocorrelations for central galaxies as a function of their stellar mass which are in good agreement with observation. The small remaining off-set may indicate a fluctuation amplitude somewhat smaller than the $\sigma_8 = 0.9$ adopted in the simulations. At yet smaller masses the large-scale correlation amplitude estimated from the SDSS disagrees with the model. Plots of

the distribution of these galaxies on the sky show that their correlations are dominated by a very small number of structures (just the Coma and Virgo clusters in the lowest mass bin) which are particularly pronounced in the minority red population. In these very shallow samples, correlation estimates are also significantly distorted by peculiar velocity effects (e.g. the finger-of-god of the Coma cluster and Virgo-centric infall). Proper accounting for these effects is beyond the scope of this paper.

At smaller separations ($r_p \leq 1$ Mpc) Fig. 20 shows substantial discrepancies between model and observation for stellar masses below $6 \times 10^{10} M_\odot$, indicating that there are more satellite–central pairs in the model than in the real data. Since the overall abundance of galaxies as a function of stellar mass matches observation very well (see Fig. 7), this discrepancy indicates that too large a fraction of the model galaxies are satellites. Again this is a clear indication favoring a lower value of σ_8 which would result in a lower abundance of the high-mass halos which host two or more galaxies in these stellar mass ranges (cf van den Bosch et al. 2007).

Additional insight into possible errors in our treatment

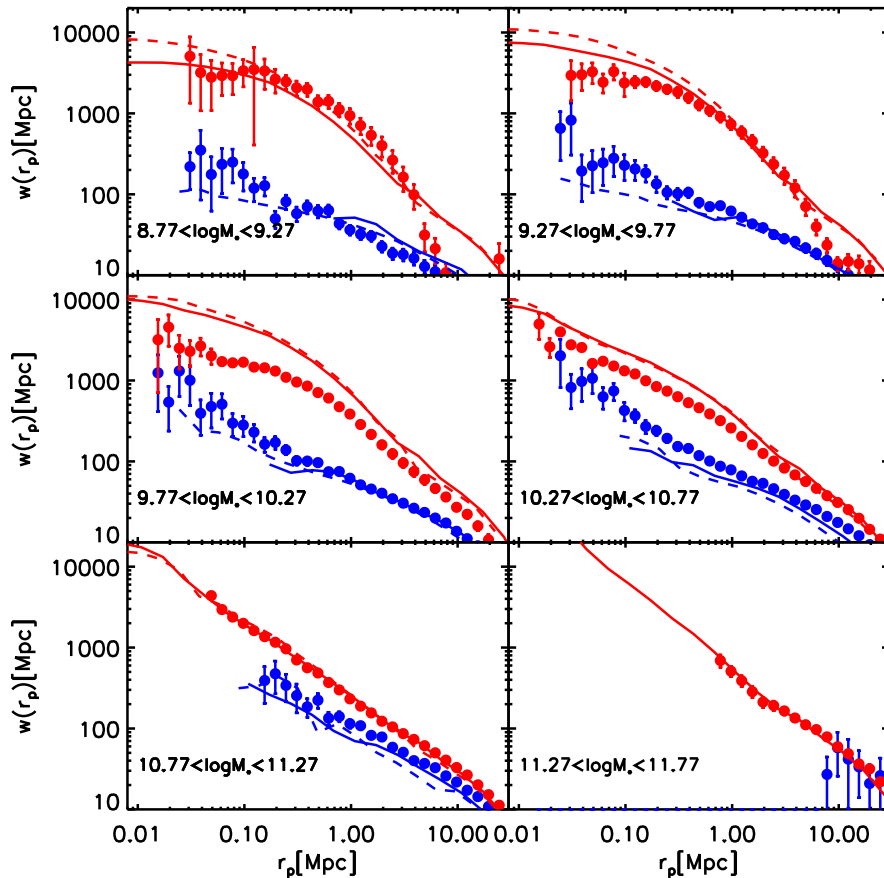


Figure 21. Projected autocorrelation functions for galaxies as a function of colour and stellar mass. As in Fig. 20, solid and dashed curves are for our preferred model applied to the MS and to the MS-II, respectively. Symbols with error bars are again derived from SDSS/DR7 using the techniques of Li et al. (2006). In each mass range, the galaxies are split into passive (red) and active (blue) subsamples according to their $g-r$ colour. The colours of the symbols and curves correspond to those of the populations. Qualitatively, the agreement between models and observations is good, with quantitative agreement at both high ($M_* > 6 \times 10^{10} M_\odot$) and low ($M_* < 6 \times 10^9 M_\odot$) stellar mass and a somewhat stronger dependence of clustering on colour than is observed at intermediate stellar masses.

of the astrophysics of galaxy evolution can be obtained by studying clustering as a function of star formation activity. To this end, Fig. 21 repeats Fig. 20 but with the galaxies in each mass range divided into “passive” (red) and “actively star-forming” (blue) subsamples according to their $g-r$ colours, as in Li et al. (2006).⁴ Lines and symbols are as in Fig. 20, except that they are coloured according to the colour of the corresponding galaxy population. As expected, red galaxies are more clustered than blue galaxies on all scales and at all stellar masses. It is encouraging that the effects are qualitatively similar in the models and in the SDSS data. Indeed, at large separation ($r_p > 2$ Mpc) there is reasonable quantitative agreement for both populations at all but the smallest stellar masses, while at large stellar mass ($M_* \geq 6 \times 10^{10} M_\odot$) there is good agreement at all separations. For active galaxies, this simply indicates once more that our halo mass – central galaxy mass relation leads to the right large-scale correlations as a function

of M_* for type 0 galaxies. For passive galaxies the situation is more complex, since most of the lower mass objects are satellites rather than centrals. Apparently, at given stellar mass, their distribution across halos of different mass is similar in the simulation and in the real world. For the two lowest mass bins the large-scale correlations are again distorted by the small volume and peculiar velocity distortion effects discussed above.

At small separations the simulations overpredict the autocorrelations of passive galaxies for stellar masses in the range $6 \times 10^9 M_\odot < M_* < 6 \times 10^{10} M_\odot$, but, curiously, the MS-II again matches the real data at lower mass. Small-scale correlations of active galaxies are underpredicted in all our lower stellar mass bins, showing that our model still has somewhat too few blue satellite galaxies. An interesting example is provided by our lowest stellar mass bin. For $2 \text{ Mpc} > r_p > 200 \text{ kpc}$ the MS-II model fits the SDSS data quite well in Fig. 21, yet lies substantially above them in Fig. 20. This is because our model overpredicts the fraction of passive galaxies in this mass range (see Fig. 11). Similar apparent discrepancies between the model/observation comparison in Fig. 21 and that in Fig. 20 are visible at a lower

⁴ For the simulations we take the division at the minimum of the “green valley” in a plot similar to Fig. 11.

level in other mass ranges, and again reflect the slightly different weightings applied in the two cases when going from colour-differentiated to “total” results.

4.10 Some properties at higher redshift

So far we have only discussed properties of our models at $z \sim 0$. This is because our observational knowledge of the galaxy population is still much more complete, more precise and less subject to systematic error in the nearby universe than at high redshift, despite the enormous recent progress in amassing data for relatively large, objectively selected samples of distant galaxies. Nevertheless, a viable galaxy formation model must be consistent not only with the present-day galaxy population, but also with that at all earlier times, so a comparison of our models with high-redshift populations is a critical part of assessing how realistically they treat the astrophysics of galaxy formation. Such work is complicated by the strong selection effects and the substantial observational uncertainties which affect the measurement of physical properties for faint and distant galaxies. As a result, detailed comparison is beyond the scope of the present paper. Earlier versions of our models have been compared to the evolution of the cosmic star-formation rate density by Croton et al. (2006), to the evolution of brightest cluster galaxies out to $z = 1$ by De Lucia & Blaizot (2007), to the galaxy counts, luminosity functions and redshift distributions inferred from deep magnitude-limited redshift surveys by Kitzbichler & White (2007) and to the abundances, redshift distributions, stellar mass distributions and clustering of colour-selected samples of $z \sim 2$ and $z \sim 3$ galaxies by Guo & White (2009). The current models can be expected to give similar results to this previous work and to be sensitive to many of the same uncertainties, notably to the treatment of dust obscuration. In this section we will limit ourselves to presenting two of the least uncertain model predictions at high redshift.

In Fig. 22 we compare the evolution of the cosmic star formation rate density predicted by our preferred model to a compilation of observational estimates taken from Hopkins (2007). The most obvious feature of this plot is a clear off-set between the model and the observations. At all redshifts the model lies a factor of two or more below the centre of the cloud of observational points. This is a reflection of the well known fact that if one integrates observational estimates of the star formation rate density with respect to time, one substantially overpredicts the observed stellar mass density, not only at $z = 0$ but also at all higher redshifts (e.g. Wilkins et al. 2008). We have chosen to adjust our model to fit the SDSS stellar mass function, so we necessarily fail to fit observational estimates of the evolution of the star formation rate density. In our model the rate of star formation peaks at $z \sim 3$ and has already declined again by a factor of 3 at $z \sim 1$, whereas the observations suggest a more constant star formation rate density over this time interval. Given the large scatter in the observational estimates and the discrepancy just discussed, it is difficult to know how seriously to take this difference. As we shall see in the next paragraph, however, there are other indications that galaxy formation occurs too early in our model, particularly for low-mass galaxies.

Stellar masses for high-redshift galaxies are notoriously

difficult to estimate because of the faintness of the images, the strong effects of dust, and the fact that the observed optical and near-IR bands correspond to the rest-frame blue and ultraviolet. The situation has improved considerably with the availability of deep data at 3.6 to 8μ from Spitzer, and according to the careful error analysis of Marchesini et al. (2009), masses with realistic error bars can now be estimated out to at least $z \sim 4$. In Fig. 23 we compare the stellar mass functions predicted by our preferred model to recent observational estimates based on combined very deep optical, near-IR and Spitzer photometry from Pérez-González et al. (2008) and Marchesini et al. (2009). We have shifted all these observational estimates so that they correspond to the same Chabrier Initial Mass Function used in our models. As Marchesini et al. (2009) describe, even with this excellent data coverage substantial random errors remain in the stellar masses estimated for individual galaxies (see also Fontanot et al. 2009). To account roughly for this, we convolve the stellar mass functions predicted by our preferred model with a gaussian of dispersion 0.25 dex in $\log M_*$ before comparing them with the observations.

Our model parameters are adjusted so that they fit the observed stellar mass function at $z \sim 0$. This good agreement is maintained out to redshifts somewhat less than unity. At higher redshift, the massive end of our predicted mass functions remains consistent with observation, once it has been convolved with the observational mass estimation uncertainties, but the abundance of lower mass galaxies ($M_* \sim 10^{10} M_\odot$) is substantially overpredicted.⁵ At face value, the discrepancy suggests that low-mass galaxies form considerably earlier in our model than in the real universe. This is consistent both with the overly high redshift of the peak of the star formation rate density (see Fig. 22) and the overly large fraction of passive galaxies in the $z \sim 0$ low-mass population (see Fig. 12). The problem is not specific to the details of our model. It has been seen in the comparison of earlier models (both our own and those of others) to this and other similar datasets (e.g. Fontana et al. 2006; Marchesini et al. 2009; Lo Faro et al. 2009; Fontanot et al. 2009; Cirasuolo et al. 2010). As several of these authors emphasise in their own discussion, the problem seems most likely to lie in the way star formation is treated in the models, particularly at high redshift.

5 DISCUSSION

New observational data at low redshift give precise measures of the abundance and clustering of galaxies as a function of their physical properties (stellar mass, luminosity, size, star formation rate, nuclear activity...) over a range of almost five orders of magnitude in stellar mass ($7 < \log M_*/M_\odot < 12$). Abundances of even lower mass galaxies are measured reasonably reliably in the Local Group. In addition, the explosion of data from ultra-deep surveys is beginning to provide convincing results for the general galaxy population at much

⁵ If the systematic error ranges discussed by Marchesini et al. (2009) are considered appropriate, this overprediction appears only marginally significant, but a large part of these systematic errors are due to possible IMF variations which we exclude for the present discussion.

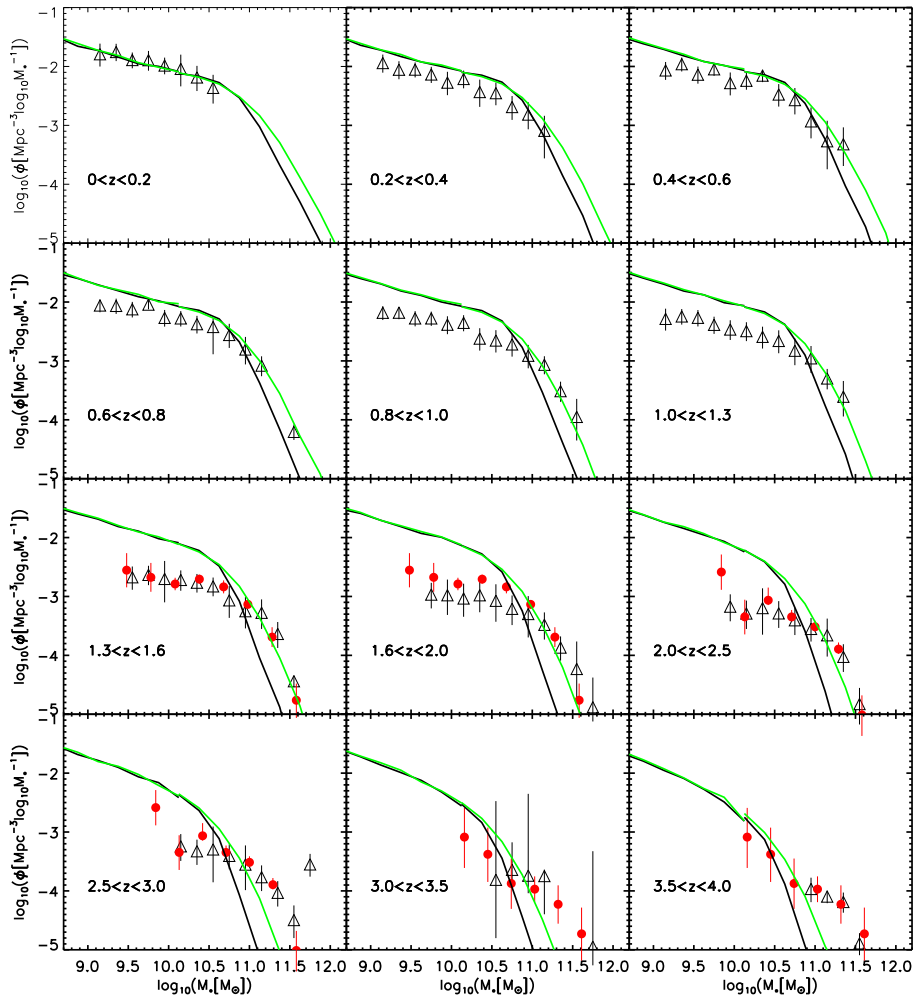


Figure 23. Stellar mass functions for a series of redshift intervals indicated by the labels in each panel. Observational data are taken from Pérez-González et al. (2008) and from Marchesini et al. (2009). Marchesini et al. (2009) compiled their mass functions for wider bins than Pérez-González et al. (2008) so in each panel we plot the Marchesini et al. (2009) results for the wider bin that includes the indicated redshift range. For the triangles representing the Pérez-González et al. (2008) data we use the error bars quoted in their paper. For the filled circles representing the Marchesini et al. (2009) results we use the error estimates which include counting statistics, cosmic variance, photometric redshift uncertainties and photometric errors, but exclude systematic uncertainties due to the IMF and other stellar population modelling issues. The mass scales of these observational results have been shifted to correct approximately to the Chabrier IMF assumed in our modelling. Black curves are the functions measured directly from the MS and the MS-II for our preferred galaxy formation model, while green curves show the result of convolving with a gaussian of dispersion 0.25 dex in $\log M_*$ in order to represent uncertainties in the individual observational stellar mass determinations.

earlier cosmic epochs. Matching such a wealth of data over such a large dynamic range is an extraordinary challenge for any *a priori* galaxy formation model. By combining results from the MS and the MS-II, and by updating and readjusting our treatments of the many relevant astrophysical processes, we have made a model which has the necessary dynamic range and statistical power to confront the full range of abundance and clustering data available at low redshift. The MS-I gives good statistics for rare, high-mass galaxies, while the MS-II provides well-resolved assembly histories for low-mass systems.

In this paper we have extended and modified our earlier treatments of the transition between the rapid infall and cooling flow regimes of gas accretion, of the sizes of bulges and of gaseous and stellar disks, of supernova feed-

back in low-mass galaxies, of the transition between central and satellite status as galaxies fall into larger systems, and of the stripping of gas and stars once they have become satellites. For physically plausible values of its parameters, the new model fits both the abundance and the large-scale clustering of low- z galaxies as a function of stellar mass, luminosity and (to a lesser extent) colour. At high mass the efficiency of star formation is limited by AGN feedback, as proposed by Croton et al. (2006). At low mass, consistency with the observed SDSS luminosity and stellar mass functions requires supernova feedback to be significantly more efficient and the reincorporation of ejected gas to be considerably less efficient than in DLB07. This enhanced SN feedback also leads to reasonable agreement with the abundance of faint satellites around the Milky Way, suggesting

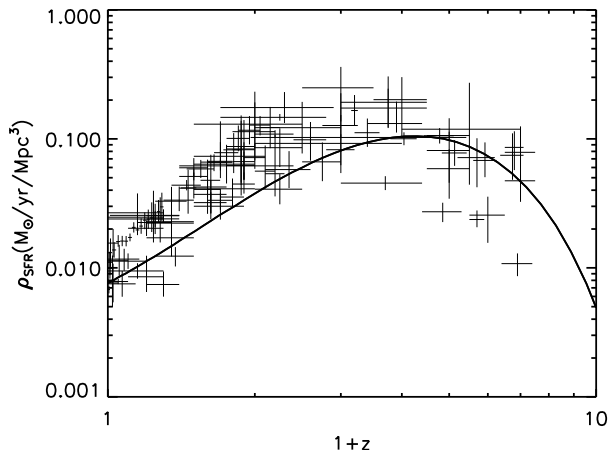


Figure 22. Cosmic star formation rate density as a function of redshift. The crosses are individual observational estimates compiled by Hopkins (2007) while the solid curve is obtained from our preferred model applied to the MS.

that reionisation influences the formation of, at most, the very smallest galaxies (see also Li et al. 2010; Macciò et al. 2010).

For galaxies of high stellar mass, our preferred model also fits both the colour distribution and the small-scale clustering of SDSS galaxies ($\log M_*/M_\odot > 9.5$ for the colours and > 10.5 for the clustering). At lower stellar mass, the model predicts a substantial fraction of red, passive galaxies which are not present in the SDSS data, and a clustering strength which rises progressively above that observed for $r_p < 1$ Mpc. (Note, however, that the *difference* in clustering between active and passive galaxies is still modelled quite accurately.) Given that our model matches both the stellar mass function and the mass-dependent large-scale clustering data from SDSS, this excessive small-scale clustering implies that too large a fraction of our galaxies are satellites at each stellar mass. Since individual groups and clusters in our model have galaxy occupation numbers and radial distributions in quite good agreement with observation, the discrepant small-scale correlations suggest that massive halos are overabundant in our simulations, i.e. that $\sigma_8 = 0.9$ is too large (c.f. van den Bosch et al. 2007). We intend to test this explicitly in future work by using the rescaling techniques of Angulo & White (2010) on the MS and MS-II so that they can be used to construct galaxy formation models very similar to those of this paper, but for cosmologies other than that originally assumed for the simulations, for example, cosmologies with lower values of σ_8 , as suggested by more recent WMAP results.

The excessive passive fraction at low stellar mass implies that our preferred model is quenching star formation in small halos in order to limit the total production of stars, whereas real objects form stars at a steady but low rate until the present day. This is also the principal reason why the model continues to have too few blue satellites, despite our improved treatment of stripping effects – at low stellar masses ($\log M_*/M_\odot < 10$) there are too few star-forming galaxies everywhere. Low-mass star-forming galaxies in the

model fit on the observed Tully-Fisher relation for isolated galaxies just as well as their giant cousins, and their large-scale clustering is also correct. Thus dwarfs appear to be forming in the proper dark halos. The overly early truncation of their star formation is very likely related to the fact that while the model correctly fits the observed abundance of massive galaxies ($M_* \sim 10^{11} M_\odot$) out to $z \sim 4$, it overpredicts the observed abundance of lower mass systems ($M_* \sim 10^{10} M_\odot$) by progressively larger amounts beyond $z \sim 0.6$. Lower mass galaxies clearly complete their formation too early in the model.

With the increased resolution provided by the MS-II we are able to show that the stellar mass function of galaxies in rich clusters is predicted to be very similar in shape to that in the general field, even down to $M_* \sim 10^7 M_\odot$. Almost all galaxies within the virial radius of a relaxed cluster are predicted to be passive, but this may be an overestimate for the reasons discussed in the last paragraph. Our new treatment of galaxy disruption suggests that 5% to 10% of all cluster stars should be part of the intracluster light, and that this fraction should increase with cluster mass and show substantial cluster to cluster variation.

The predictions for the luminosity functions and radial number count profiles of clusters are very similar in the MS and the MS-II and agree quite well with observation *provided* the substantial population of galaxies without surviving dark matter subhalos is included. Such orphan galaxies account for almost half of all cluster members with $M_* > 10^{10} M_\odot$ in the MS, and for about 13% in the MS-II. Without them the abundance of galaxies in the inner cluster would be substantially underpredicted. This demonstrates that, even at MS-II resolution, schemes that place galaxies in subhalos in a high-resolution simulation without accounting for subhalos which have been tidally disrupted but whose galaxies have survived (e.g. Vale & Ostriker 2004; Conroy et al. 2006; Wetzel et al. 2009; Moster et al. 2010; Guo et al. 2010) will not correctly reproduce the observed structure of galaxy clusters. This argument was already presented by Gao et al. (2004).

The degree to which our physically based model reproduces the observed abundance and clustering properties of the $z \sim 0$ galaxy population is impressive, but there are clear and significant discrepancies, and a comparison with high-redshift populations, although barely started here, also shows substantial discrepancies. Further work is needed to understand the source of these problems. Our simple recipes for complex astrophysical processes may turn out to be inappropriate when more accurate treatments become feasible. In addition, processes other than those we discuss may produce similar behaviour, making them operationally indistinguishable at the present level of description. Finally, there are undoubtedly degeneracies among the model parameters we have adjusted, making our specific model non-unique (see, for example, Henriques et al. 2009; Bower et al. 2010; Neistein & Weinmann 2009). Such degeneracies can only be lifted, and the recipes improved, by increasing the range, variety and precision of the data used to constrain the model.

The clearest physical indication from the results presented in this paper is that our current treatment of star formation, although similar to that used both in other phenomenological models and in direct simulations of galaxy

formation, is significantly in error, producing overly efficient star formation at early times and in small galaxies. We have tried simple modifications of these recipes but have not so far identified one which leads to substantially improved results. A better astrophysical understanding of large-scale star formation is probably required.

ACKNOWLEDGEMENTS

The halo/subhalo merger trees for the Millennium and Millennium-II Simulations are publicly available at <http://www.mpa-garching.mpg.de/millennium>, as are galaxy catalogues, galaxy merger trees and light-cone mock catalogues for previous galaxy formation models implemented on the MS. Galaxy catalogues for our new models implemented on both the MS and the MS-II will be made available on this same site as soon as this paper is accepted for publication. This Millennium site was created as part of the activities of the German Astrophysical Virtual Observatory. SW and GL acknowledge support from the European Research Council as part of the Galformod Project. GDL acknowledges financial support from the European Research Council under the European Community's Seventh Framework Programme (FP7/2007-2013)/ERC grant agreement n. 202781

REFERENCES

- Abadi M. G., Navarro J. F., Fardal M., Babul A., Steinmetz M., 2010, *MNRAS*, 407, 435
- Adami C., Picat J. P., Durret F., Mazure A., Pelló R., West M., 2007, *A&A*, 472, 749
- Aguerri J. A. L., Castro-Rodríguez N., Napolitano N., Arnaboldi M., Gerhard O., 2006, *A&A*, 457, 771
- Allen S. W., Rapetti D. A., Schmidt R. W., Ebeling H., Morris R. G., Fabian A. C., 2008, *MNRAS*, 383, 879
- Angulo R. E., White S. D. M., 2010, *MNRAS*, 405, 143
- Asplund M., Grevesse N., Sauval A. J., 2006, *Communications in Asteroseismology*, 147, 76
- Bai L., Rieke G. H., Rieke M. J., Hinz J. L., Kelly D. M., Blaylock M., 2006, *ApJ*, 639, 827
- Baldry I. K., Balogh M. L., Bower R. G., Glazebrook K., Nichol R. C., Bamford S. P., Budavari T., 2006, *MNRAS*, 373, 469
- Baldry I. K., Glazebrook K., Driver S. P., 2008, *MNRAS*, 388, 945
- Barnes J., 1984, *MNRAS*, 208, 873
- Baugh C. M., 2006, *Reports on Progress in Physics*, 69, 3101
- Baugh C. M., Lacey C. G., Frenk C. S., Granato G. L., Silva L., Bressan A., Benson A. J., Cole S., 2005, *MNRAS*, 356, 1191
- Beijersbergen M., Hoekstra H., van Dokkum P. G., van der Hulst T., 2002, *MNRAS*, 329, 385
- Belokurov V., et al. 2007, *ApJ*, 654, 897
- Benson A. J., 2010, *ArXiv e-prints*
- Benson A. J., Bower R., 2010a, *ArXiv e-prints*
- Benson A. J., Bower R., 2010b, *MNRAS*, 405, 1573
- Benson A. J., Bower R. G., Frenk C. S., Lacey C. G., Baugh C. M., Cole S., 2003, *ApJ*, 599, 38
- Benson A. J., Frenk C. S., Baugh C. M., Cole S., Lacey C. G., 2003, *MNRAS*, 343, 679
- Benson A. J., Lacey C. G., Baugh C. M., Cole S., Frenk C. S., 2002, *MNRAS*, 333, 156
- Benson A. J., Pearce F. R., Frenk C. S., Baugh C. M., Jenkins A., 2001, *MNRAS*, 320, 261
- Binggeli B., Tarengi M., Sandage A., 1990, *A&A*, 228, 42
- Binney J., Tremaine S., 1987, *Galactic dynamics*
- Binney J., Tremaine S., 2008, *Galactic Dynamics: Second Edition*. Princeton University Press
- Birnboim Y., Dekel A., 2003, *MNRAS*, 345, 349
- Birzan L., Rafferty D. A., McNamara B. R., Wise M. W., Nulsen P. E. J., 2004, *ApJ*, 607, 800
- Blanton M. R., Geha M., West A. A., 2008, *ApJ*, 682, 861
- Blanton M. R., Lupton R. H., Schlegel D. J., Strauss M. A., Brinkmann J., Fukugita M., Loveday J., 2005, *ApJ*, 631, 208
- Blumenthal G. R., Faber S. M., Flores R., Primack J. R., 1986, *ApJ*, 301, 27
- Blumenthal G. R., Faber S. M., Primack J. R., Rees M. J., 1984, *Nature*, 311, 517
- Bode P., Ostriker J. P., Turok N., 2001, *ApJ*, 556, 93
- Bower R. G., Benson A. J., Malbon R., Helly J. C., Frenk C. S., Baugh C. M., Cole S., Lacey C. G., 2006, *MNRAS*, 370, 645
- Bower R. G., McCarthy I. G., Benson A. J., 2008, *MNRAS*, 390, 1399
- Bower R. G., Vernon I., Goldstein M., Benson A. J., Lacey C. G., Baugh C. M., Cole S., Frenk C. S., 2010, *arXiv:1004.0711 [astro-ph]*
- Boyarisky A., Lesgourgues J., Ruchayskiy O., Viel M., 2009a, *Journal of Cosmology and Astro-Particle Physics*, 5, 12
- Boyarisky A., Lesgourgues J., Ruchayskiy O., Viel M., 2009b, *Physical Review Letters*, 102, 201304
- Boylan-Kolchin M., Ma C., Quataert E., 2005, *MNRAS*, 362, 184
- Boylan-Kolchin M., Ma C.-P., Quataert E., 2008, *MNRAS*, 383, 93
- Boylan-Kolchin M., Springel V., White S. D. M., Jenkins A., 2010, *MNRAS*, in press; *arXiv:0911.4484 [astro-ph]*
- Boylan-Kolchin M., Springel V., White S. D. M., Jenkins A., Lemson G., 2009, *MNRAS*, 398, 1150
- Bruzual G., Charlot S., 2003, *MNRAS*, 344, 1000
- Bullock J. S., Kravtsov A. V., Weinberg D. H., 2000, *ApJ*, 539, 517
- Cappellari M., Bacon R., Bureau M., Damen M. C., Davies R. L., de Zeeuw P. T., Emsellem E., Falcón-Barroso J., Krajnović D., Kuntschner H., McDermid R. M., Peletier R. F., Sarzi M., van den Bosch R. C. E., van de Ven G., 2006, *MNRAS*, 366, 1126
- Cattaneo A., Blaizot J., Weinberg D. H., Kereš D., Colombi S., Davé R., Devriendt J., Guiderdoni B., Katz N., 2007, *MNRAS*, 377, 63
- Cirasuolo M., McLure R. J., Dunlop J. S., Almaini O., Foucaud S., Simpson C., 2010, *MNRAS*, 401, 1166
- Cole S., Aragon-Salamanca A., Frenk C. S., Navarro J. F., Zepf S. E., 1994, *MNRAS*, 271, 781
- Cole S., Lacey C. G., Baugh C. M., Frenk C. S., 2000, *MNRAS*, 319, 168
- Colless M., et al. 2001, *MNRAS*, 328, 1039
- Conroy C., Wechsler R. H., Kravtsov A. V., 2006, *ApJ*,

- 647, 201
- Conselice C. J., 2006, MNRAS, 373, 1389
- Couchman H. M. P., Rees M. J., 1986, MNRAS, 221, 53
- Covington M., Dekel A., Cox T. J., Jonsson P., Primack J. R., 2008, MNRAS, 384, 94
- Cox T. J., Jonsson P., Somerville R. S., Primack J. R., Dekel A., 2008, MNRAS, 384, 386
- Croton D. J., Farrar G. R., 2008, MNRAS, 386, 2285
- Croton D. J., Springel V., White S. D. M., De Lucia G., Frenk C. S., Gao L., Jenkins A., Kauffmann G., Navarro J. F., Yoshida N., 2006, MNRAS, 365, 11
- Davis M., Efstathiou G., Frenk C. S., White S. D. M., 1985, ApJ, 292, 371
- De Lucia G., Blaizot J., 2007, MNRAS, 375, 2
- De Lucia G., Kauffmann G., White S. D. M., 2004, MNRAS, 349, 1101
- De Lucia G., Springel V., White S. D. M., Croton D., Kauffmann G., 2006, MNRAS, 366, 499
- Dekel A., Birnboim Y., Engel G., Freundlich J., Goerdt T., Mumcuoglu M., Neistein E., Pichon C., Teysier R., Zinger E., 2009, Nature, 457, 451
- Dekel A., Cox T. J., 2006, MNRAS, 370, 1445
- Delahaye F., Pinsonneault M. H., 2006, ApJ, 649, 529
- Diemand J., Kuhlen M., Madau P., 2007, ApJ, 657, 262
- Doroshkevich A. G., Zel'Dovich Y. B., Novikov I. D., 1967, Soviet Astronomy, 11, 233
- Dressler A., 1980, ApJ, 236, 351
- Dunkley J., Komatsu E., Nolte M. R., Spergel D. N., Larson D., Hinshaw G., Page L., Bennett C. L., Gold B., Jarosik N., Weiland J. L., Halpern M., Hill R. S., Kogut A., Limon M., Meyer S. S., Tucker G. S., Wollack E., Wright E. L., 2009, ApJS, 180, 306
- Efstathiou G., 1992, MNRAS, 256, 43P
- Efstathiou G., Lake G., Negroponte J., 1982, MNRAS, 199, 1069
- Einasto J., Saar E., Kaasik A., Chernin A. D., 1974, Nature, 252, 111
- Flynn C., Holmberg J., Portinari L., Fuchs B., Jahreiß H., 2006, MNRAS, 372, 1149
- Font A. S., Bower R. G., McCarthy I. G., Benson A. J., Frenk C. S., Helly J. C., Lacey C. G., Baugh C. M., Cole S., 2008, MNRAS, 389, 1619
- Fontana A., Salimbeni S., Grazian A., Giallongo E., Pentericci L., Nonino M., Fontanot F., Menci N., Monaco P., Cristiani S., Vanzella E., de Santis C., Galozzi S., 2006, A&A, 459, 745
- Fontanot F., De Lucia G., Monaco P., Somerville R. S., Santini P., 2009, MNRAS, 397, 1776
- Forcada-Miro M. I., White S. D. M., 1997, arXiv:astro-ph/9712204
- Fu L. e. a., 2008, A&A, 479, 9
- Gao L., De Lucia G., White S. D. M., Jenkins A., 2004, MNRAS, 352, L1
- Gerhard O., Arnaboldi M., Freeman K. C., Kashikawa N., Okamura S., Yasuda N., 2005, ApJ, 621, L93
- Gnedin N. Y., 2000, ApJ, 542, 535
- Gnedin N. Y., Kravtsov A. V., 2006, ApJ, 645, 1054
- Gnedin O. Y., Kravtsov A. V., Klypin A. A., Nagai D., 2004, ApJ, 616, 16
- Gonzalez A. H., Zabludoff A. I., Zaritsky D., 2005, ApJ, 618, 195
- Gonzalez A. H., Zaritsky D., Zabludoff A. I., 2007, ApJ, 666, 147
- Guo Q., White S., Li C., Boylan-Kolchin M., 2010, MNRAS, 404, 1111
- Guo Q., White S. D. M., 2009, MNRAS, 396, 39
- Hambrick D. C., Ostriker J. P., Naab T., Johansson P. H., 2009, ApJ, 705, 1566
- Hansen S. M., Sheldon E. S., Wechsler R. H., Koester B. P., 2009, ApJ, 699, 1333
- Håring N., Rix H., 2004, ApJ, 604, L89
- Hatton S., Devriendt J. E. G., Ninin S., Bouchet F. R., Guiderdoni B., Vibert D., 2003, MNRAS, 343, 75
- Hayashi E., Navarro J. F., Taylor J. E., Stadel J., Quinn T., 2003, ApJ, 584, 541
- Henriques B. M. B., Thomas P. A., Oliver S., Roseboom I., 2009, MNRAS, 396, 535
- Hoefl M., Yepes G., Gottlöber S., Springel V., 2006, MNRAS, 371, 401
- Hopkins A. M., 2007, in J. Afonso, H. C. Ferguson, B. Mobasher, & R. Norris ed., *Deepest Astronomical Surveys Vol. 380 of Astronomical Society of the Pacific Conference Series, The Star Formation History of the Universe*. pp 423–+
- Hopkins P. F., Hernquist L., Cox T. J., Keres D., Wuyts S., 2009, ApJ, 691, 1424
- Jeltema T. E., Binder B., Mulchaey J. S., 2008, ApJ, 679, 1162
- Jenkins L. P., Hornschemeier A. E., Mobasher B., Alexander D. M., Bauer F. E., 2007, ApJ, 666, 846
- Jiang C. Y., Jing Y. P., Faltenbacher A., Lin W. P., Li C., 2008, ApJ, 675, 1095
- Kang X., Jing Y. P., Mo H. J., Börner G., 2005, ApJ, 631, 21
- Kauffmann G., 1996, MNRAS, 281, 487
- Kauffmann G., Colberg J. M., Diaferio A., White S. D. M., 1999, MNRAS, 303, 188
- Kauffmann G., White S. D. M., Guiderdoni B., 1993, MNRAS, 264, 201
- Kazantzidis S., Mayer L., Mastropietro C., Diemand J., Stadel J., Moore B., 2004, ApJ, 608, 663
- Kennicutt Jr. R. C., 1998, ApJ, 498, 541
- Kitzbichler M. G., White S. D. M., 2007, MNRAS, 376, 2
- Klypin A., Gottlöber S., Kravtsov A. V., Khokhlov A. M., 1999, ApJ, 516, 530
- Komatsu E., Smith K. M., Dunkley J., Bennett C. L., Gold B., Hinshaw G., Jarosik N., Larson et al. 2010, ArXiv e-prints
- Koposov S., Belokurov V., Evans N. W., Hewett P. C., Irwin M. J., Gilmore G., Zucker D. B., Rix H.-W., Fellhauer M., Bell E. F., Glushkova E. V., 2008, ApJ, 686, 279
- Kravtsov A. V., Gnedin O. Y., Klypin A. A., 2004, ApJ, 609, 482
- Larson R. B., 1974, MNRAS, 169, 229
- Lee H., Skillman E. D., Cannon J. M., Jackson D. C., Gehrz R. D., Polonski E. F., Woodward C. E., 2006, ApJ, 647, 970
- Li C., Kauffmann G., Jing Y. P., White S. D. M., Börner G., Cheng F. Z., 2006, MNRAS, 368, 21
- Li C., White S. D. M., 2009, MNRAS, 398, 2177
- Li Y., De Lucia G., Helmi A., 2010, MNRAS, 401, 2036
- Lo Faro B., Monaco P., Vanzella E., Fontanot F., Silva L., Cristiani S., 2009, MNRAS, 399, 827

- Macciò A. V., Kang X., Fontanot F., Somerville R. S., Koposov S., Monaco P., 2010, *MNRAS*, 402, 1995
- Marchesini D., van Dokkum P. G., Förster Schreiber N. M., Franx M., Labbé I., Wuyts S., 2009, *ApJ*, 701, 1765
- McCarthy I. G., Frenk C. S., Font A. S., Lacey C. G., Bower R. G., Mitchell N. L., Balogh M. L., Theuns T., 2008, *MNRAS*, 383, 593
- McGee S. L., Balogh M. L., 2010, *MNRAS*, pp L21+
- McNamara B. R., Nulsen P. E. J., 2007, *ARA&A*, 45, 117
- Mihos J. C., Harding P., Feldmeier J., Morrison H., 2005, *ApJ*, 631, L41
- Milne M. L., Pritchett C. J., Poole G. B., Gwyn S. D. J., Kavelaars J. J., Harris W. E., Hanes D. A., 2007, *AJ*, 133, 177
- Mo H. J., Mao S., White S. D. M., 1998, *MNRAS*, 295, 319
- Mobasher B., Colless M., Carter D., Poggianti B. M., Bridges T. J., Kranz K., Komiyama Y., Kashikawa N., Yagi M., Okamura S., 2003, *ApJ*, 587, 605
- Moore B., Ghigna S., Governato F., Lake G., Quinn T., Stadel J., Tozzi P., 1999, *ApJ*, 524, L19
- More S., van den Bosch F. C., Cacciato M., Mo H. J., Yang X., Li R., 2009, *MNRAS*, 392, 801
- Moster B. P., Somerville R. S., Maulbetsch C., van den Bosch F. C., Macciò A. V., Naab T., Oser L., 2010, *ApJ*, 710, 903
- Naab T., Burkert A., 2003, *ApJ*, 597, 893
- Nair P. B., van den Bergh S., Abraham R. G., 2010, *ApJ*, 715, 606
- Navarro J. F., Steinmetz M., 1997, *ApJ*, 478, 13
- Navarro J. F., Steinmetz M., 2000, *ApJ*, 528, 607
- Neistein E., Weinmann S. M., 2009, *ArXiv* 0911.3147
- Noordermeer E., van der Hulst J. M., Sancisi R., Swaters R. A., van Albada T. S., 2005, *A&A*, 442, 137
- Okamoto T., Frenk C. S., Jenkins A., Theuns T., 2010, *MNRAS*, 406, 208
- Okamoto T., Gao L., Theuns T., 2008, *MNRAS*, 390, 920
- Paschos P., Jena T., Tytler D., Kirkman D., Norman M. L., 2009, *MNRAS*, 399, 1934
- Peng Y., et al. 2010, *arXiv:1003.4747* [astro-ph]
- Percival W. J. e. a., 2010, *MNRAS*, 401, 2148
- Pérez-González P. G., Rieke G. H., Villar V., Barro G., Blaylock M., Egami E., Gallego J., Gil de Paz A., Pascual S., Zamorano J., Donley J. L., 2008, *ApJ*, 675, 234
- Popesso P., Biviano A., Böhringer H., Romaniello M., 2006, *A&A*, 445, 29
- Quadri R. F., Williams R. J., Lee K., Franx M., van Dokkum P., Brammer G. B., 2008, *ApJ*, 685, L1
- Rees M. J., Ostriker J. P., 1977, *MNRAS*, 179, 541
- Sawala T., Scannapieco C., Maio U., White S., 2010, *MNRAS*, 402, 1599
- Sellwood J. A., Evans N. W., 2001, *ApJ*, 546, 176
- Sellwood J. A., Moore E. M., 1999, *ApJ*, 510, 125
- Shen S., Mo H. J., White S. D. M., Blanton M. R., Kauffmann G., Voges W., Brinkmann J., Csabai I., 2003, *MNRAS*, 343, 978
- Silk J., Rees M. J., 1998, *A&A*, 331, L1
- Somerville R. S., 2002, *ApJ*, 572, L23
- Somerville R. S., Hopkins P. F., Cox T. J., Robertson B. E., Hernquist L., 2008, *MNRAS*, 391, 481
- Somerville R. S., Primack J. R., 1999, *MNRAS*, 310, 1087
- Somerville R. S., Primack J. R., Faber S. M., 2001, *MNRAS*, 320, 504
- Spergel D. N., Verde L., Peiris H. V., Komatsu E., et al. 2003, *ApJS*, 148, 175
- Springel V., Hernquist L., 2003, *MNRAS*, 339, 312
- Springel V., Wang J., Vogelsberger M., Ludlow A., Jenkins A., Helmi A., Navarro J. F., Frenk C. S., White S. D. M., 2008, *MNRAS*, 391, 1685
- Springel V., White S. D. M., Jenkins A., Frenk C. S., Yoshida N., Gao L., Navarro J., Thacker R., Croton D., Helly J., Peacock J. A., Cole S., Thomas P., Couchman H., Evrard A., Colberg J., Pearce F., 2005, *Nature*, 435, 629
- Springel V., White S. D. M., Tormen G., Kauffmann G., 2001, *MNRAS*, 328, 726
- Springob C. M., Masters K. L., Haynes M. P., Giovanelli R., Marinoni C., 2007, *ApJS*, 172, 599
- Steidel C. C., Shapley A. E., Pettini M., Adelberger K. L., Erb D. K., Reddy N. A., Hunt M. P., 2004, *ApJ*, 604, 534
- Steinmetz M., 1999, *Ap&SS*, 269, 513
- Sun M., Jones C., Forman W., Vikhlinin A., Donahue M., Voit M., 2007, *ApJ*, 657, 197
- Sutherland R. S., Dopita M. A., 1993, *ApJS*, 88, 253
- Tissera P. B., White S. D. M., Pedrosa S., Scannapieco C., 2010, *MNRAS*, 406, 922
- Toomre A., 1964, *ApJ*, 139, 1217
- Tremonti C. A., Heckman T. M., Kauffmann G., Brinchmann J., Charlot S., White S. D. M., Seibert M., Peng E. W., Schlegel D. J., Uomoto A., Fukugita M., Brinkmann J., 2004, *ApJ*, 613, 898
- Vale A., Ostriker J. P., 2004, *MNRAS*, 353, 189
- van den Bosch F. C., Yang X., Mo H. J., Weinmann S. M., Macciò A. V., More S., Cacciato M., Skibba R., Kang X., 2007, *MNRAS*, 376, 841
- Viel M., Becker G. D., Bolton J. S., Haehnelt M. G., Rauch M., Sargent W. L. W., 2008, *Physical Review Letters*, 100, 041304
- Viel M., Bolton J. S., Haehnelt M. G., 2009, *MNRAS*, 399, L39
- Vikhlinin A., Kravtsov A. V., Burenin R. A., Ebeling H., Forman W. R., Hornstrup A., Jones C., Murray S. S., Nagai D., Quintana H., Voevodkin A., 2009, *ApJ*, 692, 1060
- von der Linden A., Best P. N., Kauffmann G., White S. D. M., 2007, *MNRAS*, 379, 867
- Wang L., Li C., Kauffmann G., De Lucia G., 2006, *MNRAS*, 371, 537
- Wang L., Li C., Kauffmann G., De Lucia G., 2007, *MNRAS*, 377, 1419
- Weinmann S. M., Kauffmann G., von der Linden A., De Lucia G., 2009, *arXiv:0912.2741* [astro-ph]
- Weinmann S. M., van den Bosch F. C., Yang X., Mo H. J., Croton D. J., Moore B., 2006, *MNRAS*, 372, 1161
- Wetzell A. R., Cohn J. D., White M., 2009, *MNRAS*, 395, 1376
- White S. D. M., Frenk C. S., 1991, *ApJ*, 379, 52
- White S. D. M., Rees M. J., 1978, *MNRAS*, 183, 341
- Wilkins S. M., Trentham N., Hopkins A. M., 2008, *MNRAS*, 385, 687
- Willman B., Dalcanton J. J., Martinez-Delgado D., West A. A., Blanton M. R., Hogg D. W., Barentine J. C., Brewington H. J., Harvanek M., Kleinman S. J., Krzesinski J., Long D., Neilsen Jr. E. H., Nitta A., Snedden S. A., 2005, *ApJ*, 626, L85

Yoshida N., Stoehr F., Springel V., White S. D. M., 2002, MNRAS, 335, 762

Zabludoff A. I., Zaritsky D., Lin H., Tucker D., Hashimoto Y., Shectman S. A., Oemler A., Kirshner R. P., 1996, ApJ, 466, 104

Zavala J., Jing Y. P., Faltenbacher A., Yepes G., Hoffman Y., Gottlöber S., Catinella B., 2009, ApJ, 700, 1779

Zibetti S., White S. D. M., Schneider D. P., Brinkmann J., 2005, MNRAS, 358, 949

Zucker D. B., et al. 2006, ApJ, 643, L103

APPENDIX A

As discussed in Sec. 3.6, we have modified our previous treatment of the transition between central and satellite status when galaxies fall into larger systems. As long as the subhalo associated with a galaxy remains outside the virial radius of its FOF group, we now continue to treat that galaxy as an independent central object. Thus galaxies effectively become satellites only when they fall within R_{vir} . This reduces the number of satellites from the point of view of our galaxy formation modelling and it increases the fraction of satellites which are type 2 or “orphan” systems with no associated subhalo. (This is because the orphans almost all lie within R_{vir} .) Here we illustrate the change in the effective number of satellites in our two simulations as a function of stellar mass.

Fig. 24 shows the fraction of all galaxies at each stellar mass which are satellite systems of various types. Red curves refer to the MS-II and are plotted down to a stellar mass of $10^7 M_{\odot}$, while blue curves refer to the MS and stop at its resolution limit, $M_{*} \sim 10^{9.5} M_{\odot}$. For each simulation the solid curve gives the fraction of galaxies which are centred on non-dominant subhalos of their FOF groups, the dashed curve gives the fraction which are in addition within R_{vir} , and the upper and lower dotted curves give the fractions which are orphans within FOF groups and within R_{vir} , respectively. In our previous work (e.g. DLB07) the galaxies corresponding to the solid and upper dotted curves were treated as satellites when modelling their evolution. In the current paper it is rather the galaxies corresponding to the dashed and lower dotted curves which are treated as satellites; the galaxies corresponding to the difference between the solid and dashed curves continue to be treated as centrals. Thus the effective satellite fraction is smaller in this paper than in our previous work. Notice that while the improved resolution of the MS-II does decrease the number of orphan galaxies in comparison to the MS, these remain a significant population, even at relatively high stellar mass. Notice also that above the mass limit of the MS, the total fraction of galaxies which are satellites agrees well between the two simulations, demonstrating that our treatment of orphans in the MS is indeed appropriate, as also concluded earlier when discussing Fig.14.

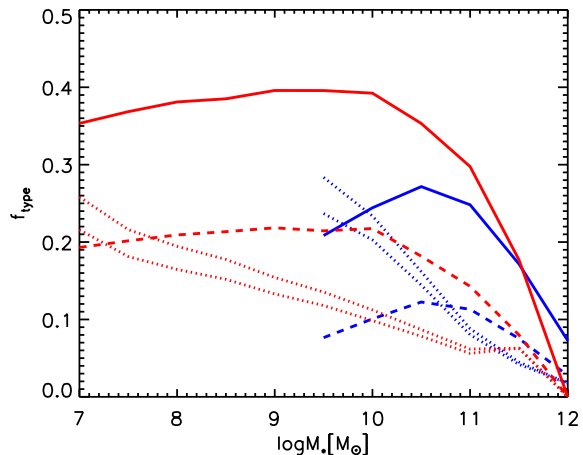


Figure 24. The fraction of all galaxies which are satellites of various types as a function of stellar mass. Blue curves are results for the MS and red curves for the MS-II. For each simulation and at each stellar mass, a solid curve gives the fraction centred on a non-dominant, satellite subhalo (type 1 galaxies), a dashed curve gives the fraction which are in addition within R_{vir} of halo centre, and dotted curves give the fraction with no remaining associated subhalo (type 2 or “orphan” satellites; the upper curve refers to orphans within the FOF group while the lower only counts orphans within R_{vir}). Note that in both simulations a substantial fraction of the type 1’s are actually outside R_{vir} and so continue to be treated as central galaxies by our modified prescriptions. Note also that while improved resolution reduces the number of orphans in the MS-II, they remain a significant population even at relatively large stellar mass.